Soft Matter

# Multilayered Ordered Arrays Self-Assembled from a Mixed Population of Nanoparticles



| | |
|---|---|
| Journal: | *Soft Matter* |
| Manuscript ID | SM-ART-11-2024-001370.R1 |
| Article Type: | Paper |
| Date Submitted by the Author: | 05-Mar-2025 |
| Complete List of Authors: | Faccini de Lima, Camila; Indiana University, Intelligent Systems Engineering<br>Hewagama, Nathasha; Indiana University Bloomington<br>Uchida, Masaki; California State University Fresno<br>Douglas, Trevor; Indiana University, Department of Chemistry<br>Jadhao, Vikram; Indiana University Bloomington, |
| | |

Soft Matter

ARTICLE TYPE

Cite this: DOI: 00.0000/xxxxxxxxxx

# Multilayered Ordered Arrays Self-Assembled from a Mixed Population of Nanoparticles

Camila Faccini de Lima,[a] Nathasha D. Hewagama,[b] Masaki Uchida,[c] Trevor Douglas,*[b] and Vikram Jadhao *[a]

Received Date
Accepted Date

DOI: 00.0000/xxxxxxxxxx

An experimentally-informed coarse-grained model is presented to probe the self-assembly of multiple types of charged nanoparticles in a one-pot mixture in the presence of oppositely charged linkers across a broad range of nanoparticle charge and ionic strength of the solution. The model is applied to study the self-assembly of negatively-charged bacteriophage P22 virus-like particles (VLPs) of different types, with each type comprising VLPs of a distinct surface charge, in the presence of positively-charged PAMAM G6 dendrimers. The model accurately captures the self-assembly of one-component systems, including the assembly states of the highest-charged P22 variant that were inaccessible with earlier models, revealing that P22 VLPs assemble into ordered arrays below a threshold ionic strength that increases with increasing variant charge, consistent with experiments. Molecular dynamics simulations of two, three, and four-component mixtures of P22 VLPs show that changing the ionic strength gradually over the range of well separated threshold ionic strengths via dialysis generates hierarchical assembly of ordered multilayered core-shell structures, with each layer comprising VLPs of a single variant type. A quick decrease in the ionic strength via rapid dilution leads to amorphous aggregates with a mixed composition of different variants. The mechanisms driving the VLPs into different macrostructures are explored by examining the bound and bridging dendrimers associated with the different types of VLPs. Simulation findings are consistent with experiments and establish salt dialysis as a simple and versatile strategy to engineer multilayered and ordered structures via a single-pot synthesis of multiple types of nanoscale building blocks.

## 1 Introduction

From the crystal structure of a ribosome[1] to viral capsids and protein cages[2], self-assembly is a key principle in nature for the creation of complex structures at the nanoscale[3,4]. Inspired by nature, scientists have explored self-assembly as a bottom-up approach to organize nanoscale building blocks into diverse types of synthetic functional materials with optical, electromagnetic, and biomimetic properties[5–8]. Examples include nanocontainers for drug delivery[2], three-dimensional (3D) electrical networks[9], photonic crystals[10], field-effect transistors[11], among others[12–14].

Many studies have focused on realizing the bottom-up assembly of nanoparticles (NPs) into hierarchically organized 3D structures[15–20] that can exhibit enhanced properties and functions compared to their individual building blocks. This assembly engineering often involves tailoring the shape, size, and surface composition of NPs with specific features[21–27], and modulating the NP environment[28–31]. Protein-based materials such as virus-like particles (VLPs) have attracted a lot of interest as building block NPs[28,32–37]. VLPs are protein cages with a well-defined geometry that are derived often from biological viruses by co-opting the viral capsid's robust self-assembly process from a few protein subunits[2,38,39]. They can reliably assemble into NPs that exhibit a high degree of shape and size monodispersity. Further, their surface can be engineered to alter features such as charge, polarity, and hydrophobicity via chemical or genetic modifications[40–43]. These attributes make VLPs ideal as scaffolds for bottom-up hierarchical assembly engineering. Additionally, a variety of cargoes including active enzymes and smaller inorganic NPs can be encapsulated into individual VLPs[2,28,44]. Hierarchical assembly of VLPs into superstructures opens design strategies for fabricating novel plasmonic metamaterials and catalytic systems that can exhibit collective functions, e.g., coupled catalysis[29,45,46].

The assembly of VLPs into 3D ordered structures has been realized using electrostatic, hydrophobic, complementary DNA hybridization, and specific protein-protein interac-

[a] *Intelligent Systems Engineering, Indiana University, Bloomington, Indiana 47408, USA*
[b] *Department of Chemistry, Indiana University, Bloomington, Indiana 47405, USA*
[c] *Department of Chemistry and Biochemistry, California State University, Fresno, California 93740, USA*

† Supplementary Information available: [details of any supplementary information available should be included here]. See DOI: 10.1039/cXsm00000x/

tions[28,29,32,34,46–52]. For example, the assembly of Simian Virus 40 VLPs into BCC crystal structures was driven by electrostatic interactions modulated by magnesium ions[52]. The self-assembly process is often mediated using linker macromolecules such as polymers and smaller NPs[8,28,29,33,46,47]. For example, superlattices with FCC crystalline order were self-assembled from cowpea chlorotic mottle (CCMV) VLPs using different types of oppositely-charged linkers including gold NPs[47] and polymers such as first-generation Newkome-type dendron and first-generation polyamidoamine (PAMAM) dendrimers[8].

VLPs derived from the bacteriophage P22 have been utilized as a building block by many researchers for generating hierarchical assemblies[28,29,33,46,51]. The P22 VLP is an icosahedral capsid of $\approx 56$ nm diameter that offers versatility in the encapsulation of a wide range of functional cargoes[28,53–55]. Higher-order assembly of P22 VLPs was realized using biological linker molecules engineered from the capsid decoration protein (Dec), which binds to symmetry-specific sites on the viral capsid[46]. P22 VLPs were self-assembled into ordered superlattices using inorganic NPs and generation-3 (G3) PAMAM dendrimers as rigid and soft linker materials respectively, with NaCl salt solution controlling the VLP-linker electrostatic interactions driving the assembly process[33]. Our earlier work employing small angle X-ray scattering (SAXS) experiments and molecular dynamics (MD) simulations demonstrated that P22 VLP variants, genetically engineered to exhibit different surface charges, spontaneously assemble into ordered arrays with FCC/HCP structure in the presence of oppositely-charged generation-6 (G6) PAMAM dendrimers[28,29,51]. Assembly of different variants into ordered arrays was observed when the ionic strength was decreased below a threshold value, which increased with increasing the variant charge.

Realizing hierarchical self-assembled structures starting from a mixture of multiple types of NPs have also received attention[21,34,47], however, it continues to be a challenge to control the spatial arrangement of many distinct types of building blocks when assembling them into 3D layered materials. Recently, we demonstrated using experiments and simulations that two-component mixtures of P22 VLP variants can self-assemble into ordered and layered core-shell arrays, where each layer is composed of a single type of VLPs, via a dialysis-based modulation of the solution's ionic strength[56]. Experiments showed that the dialysis approach can be extended to generate multilayered core-shell structures in mixtures of 4 types of P22 variants[56].

In this paper, we develop a coarse-grained model to capture the self-assembly of charged NPs in the presence of oppositely charged linker macromolecules over a broad range of NP charges and salt concentrations, and apply the model to probe the assembly of different two, three, and four-component VLP mixtures in the presence of G6 PAMAM dendrimers. We introduce a charge-dependent proximity parameter to characterize the VLP-linker steric interaction, which enables the application of the model to probe the self-assembly of single-component systems associated with highly-charged P22 variants. MD simulations of mixtures of multiple types of VLPs show that changing the ionic strength gradually via dialysis establishes an electrostatic drive to selectively assemble VLPs of one type, characterized by the same surface charge, leading to hierarchical assembly of ordered multilayered core-shell structures. Reducing the ionic strength quickly via rapid dilution produces amorphous aggregates with a mixed composition of VLPs of different types. Simulation results are validated by imaging and scattering experiments.

The differences in order characterizing the self-assembled structures resulting from dialysis vs rapid dilution of the VLP solutions are characterized using VLP-VLP self and cross pair correlation functions. Simulations show that the method of ionic strength control has a profound influence on the recruitment of dendrimers that act as bridges between the VLPs. The higher-charged VLPs are found to alter the assembly pathways of the lower-charged VLPs, leading to their aggregation at ionic strengths higher than the threshold values established via the assembly of one-component systems. This aggregation is attributed to the enhanced recruitment of bound and bridging dendrimers by the lower-charged VLPs aided by the presence of the higher-charged VLPs. These findings establish a bottom-up strategy to synthesize multilayered materials by controlling the spatial arrangement of mixed populations of NPs in a one-pot fabrication. The hierarchical organization of NPs of multiple types in a single superstructure opens pathways to engineer complex nanomaterials with tunable multifunctional properties for drug delivery, biomimetic catalysts, and sensing applications.

## 2 Models and Methods

This section describes the new coarse-grained model and provides the details of the simulation techniques and protocols. The reader is referred to our previous publication for the details of the experimental methods to prepare P22 VLP variants, image the assembled constructs using 3D structured illumination microscopy (SIM), and identify the structure using SAXS measurements[56].

### 2.1 Coarse-grained model

A coarse-grained model of the NP-linker system is developed based on the models employed in our earlier work[29,56] with the goal of extending the application to NPs with large surface charge and solutions of high ionic strength in order to enable the study of a large variety of multi-component mixtures. The model is tailored for the system of P22 VLPs (NPs) and G6 PAMAM dendrimers (linkers) in an aqueous solution with added salt. VLPs associated with 4 P22 variants: P22-EEE2, P22-E2, P22-Q2, and P22-K2, are modeled as uniformly-charged, hollow spheres of mass 20 MDa and diameter 56 nm[29,56]. The VLP surface charge $q_v$ changes with the variant type as evidenced by the different experimentally measured $\zeta$ potential values (Table 1). P22-E2 VLPs are assigned a charge of $-1500e$ following an empirical approach described in our previous paper[29] which involved monitoring the dendrimer-mediated assembly behavior of P22-E2 VLPs in simulations over a range of VLP and dendrimer charge values near the experimentally observed ionic strength threshold ($\approx 250$ mM), and ensuring consistency between experiment and simulation results. $q_v$ is assumed to scale linearly with the $\zeta$ potential, and the strength of the $\zeta$ potentials of other variants relative to that of the E2 variant are assumed to be the same as that measured at

Table 1 P22 variant type and the associated zeta potential $\zeta$, charge $q_v$, proximity parameter $\sigma_{hc}$, and threshold ionic strength estimated using experiments ($I_t^{\text{expt}}$) and simulations ($I_t^{\text{sim}}$)

| P22 variant | $\zeta$ (mV) | $q_v$ (e) | $\sigma_{hc}$ (nm) | $I_t^{\text{expt}}$ (mM) | $I_t^{\text{sim}}$ (mM) |
|---|---|---|---|---|---|
| K2 | $-12.8$ | $-622$ | 4 | $61.7 \pm 20$ | 75 |
| Q2 | $-23.6$ | $-1165$ | 4 | $123 \pm 20$ | 160 |
| E2 | $-30.4$ | $-1500$ | 5.16 | $247 \pm 20$ | 245 |
| EEE2 | $-43.0$ | $-2122$ | 5.16 | $555 \pm 20$ | 550 |

41.1 mM, which determines the acceptable range for the charge of the 3 other variants. Following this process, P22-EEE2, P22-E2, P22-Q2, and P22-K2 VLPs are assigned charges of $q_v = -2122e$, $-1500e$, $-1165e$, and $-622e$ respectively. Dendrimers are modeled as positively-charged spheres of mass 0.058 MDa and diameter 6.7 nm following the reported experimental measurements of their hydrodynamic diameter[57], and they are assigned a charge $q_d = 45e$ following the aforementioned empirical approach[56].

While using the same $q_v$ and $q_d$ over the range of salt concentrations considered here enables an effective minimal model representation, $q_v$ and $q_d$ can change with salt concentration[58,59]. Considering the relatively high ionic strengths and small VLP packing fraction ($\approx 0.02$) probed in simulations, which leads to $O(100,000)$ ion pairs per VLP, we expect the change of VLP effective charge with salt to be a minor effect except for the smallest ionic strengths probed in our study, with the largest correction coming for the EEE2 variant for $I \lesssim 100$ mM[60]. Our capacity to estimate the variability of effective charges of dendrimers as a function of ionic strength is limited because of the dendritic topology effects neglected in our model and the associated uncertainty in estimating the salt-dependent dissociation cost of counterions buried deep in the dendritic structure.

The solvent is treated as a continuous medium and its effect is incorporated in the coarse-grained model by scaling the electrostatic interactions by the relative dielectric permittivity $\varepsilon_r$ of the solvent. The effects of salt ions are also taken into account implicitly via a screened Coulomb (Yukawa-type) potential characterized by a Debye length $\lambda_D$ which depends on the ionic strength $I$ of the solution. Utilizing these approximations, the effective electrostatic interactions between each pair $(i,j)$ of particles separated by a center-to-center distance $r_{ij} = r$ are modeled as:

$$u_Y(r) = \frac{q_i e^{\kappa\sigma_i/2}}{(1+\kappa\sigma_i/2)} \frac{q_j e^{\kappa\sigma_j/2}}{(1+\kappa\sigma_j/2)} \frac{l_B e^{-\kappa r}}{r} \tag{1}$$

where $q_i, q_j$ are the surface charges and $\sigma_i, \sigma_j$ are the diameters associated with the $i^{\text{th}}$ and $j^{\text{th}}$ particles respectively. $u_Y$ is expressed in units of $k_BT$ by introducing the Bjerrum length $l_B = e^2/(4\pi\varepsilon_0\varepsilon_r k_B T)$, where $\varepsilon_0$ is the vacuum permittivity, $k_B$ is the Boltzmann constant, and $T$ is the temperature. For water at $T = 298$ K, $\varepsilon_r = 78.5$ and $l_B = 0.714$ nm. In Equation 1, $\kappa = \lambda_D^{-1} = \sqrt{8\pi l_B I}$. $\lambda_D$ varied between $\approx 3$ nm and $\approx 0.4$ nm over the range of ionic strength $I \in (10,600)$ mM probed in this work.

The steric interactions between a pair of VLPs or dendrimers are modeled using the standard, truncated and shifted purely-repulsive Lennard-Jones (LJ) potential:

$$u_{LJ}(r) = 4\left[\left(\frac{\sigma}{r}\right)^{12} - \left(\frac{\sigma}{r}\right)^{6}\right] + 1, \quad r < 2^{1/6}\sigma \tag{2}$$

where $\sigma$ is the particle (VLP or dendrimer) diameter. For $r \geq 2^{1/6}\sigma$, $u_{LJ}(r) = 0$. In Equation 2, the characteristic LJ bond energy parameter $\varepsilon_{LJ} = 1\, k_BT$ and $u_{LJ}$ is expressed in units of $k_BT$.

P22 VLPs are significantly larger, by $\approx 8\times$, compared to the dendrimers. This size disparity is common in NP-linker systems where linkers mediate the assembly of NPs into higher-order structures[4,61,62]. Inspired by the models developed to study systems of oppositely-charged particles with different sizes[63,64], the steric interaction between a VLP and a dendrimer separated by a distance $r$ is modeled by an impenetrable hard-core potential $u_{mLJ}(r) = \infty$ for $r \leq \Delta$, by a purely-repulsive modified LJ potential:

$$u_{mLJ}(r) = 4\left[\left(\frac{\sigma_{hc}}{r-\Delta}\right)^{12} - \left(\frac{\sigma_{hc}}{r-\Delta}\right)^{6}\right] + 1 \tag{3}$$

for $\Delta < r < \Delta + 2^{1/6}\sigma_{hc}$, and as $u_{mLJ}(r) = 0$ for $r \geq \Delta + 2^{1/6}\sigma_{hc}$. Here, $u_{mLJ}$ is in units of $k_BT$ and $\Delta = (\sigma_v + \sigma_d)/2 - \sigma_{hc}$ is the hard-core diameter, where $\sigma_v$ is the VLP diameter and $\sigma_d$ is the dendrimer diameter. The parameter $\sigma_{hc}$ modulates the hardness of the repulsive interactions, which controls the extent to which dendrimers may approach the VLPs, as discussed in detail below.

### 2.2 Selecting proximity parameter $\sigma_{hc}$

The electrostatic attraction $u_Y$ between a VLP and a dendrimer sets up a favorable energetic drive for a dendrimer to be in the vicinity of a VLP. This drive is countered by the steric repulsion between VLP and dendrimer produced by $u_{mLJ}$. Changing $\sigma_{hc}$ modulates this repulsion and alters the net potential energy $u_{net}(r) = u_Y(r) + u_{mLJ}(r)$ driving the dendrimer closer to the VLP. The effect of changing $\sigma_{hc}$ on $u_{net}(r)$ is illustrated in Figure 1(a) for the case of a dendrimer interacting with a P22-E2 VLP at an ionic strength $I = 240$ mM near the experimentally observed ionic strength threshold for the E2 VLPs to assemble into ordered arrays. Tuning $\sigma_{hc}$ alters the distance associated with the minimum of $u_{net}(r)$, also called the distance of closest approach $r_c$, and the value of the net potential $u_{net}^{min} = u_{net}(r_c)$ at $r_c$.

The choice of $\sigma_{hc}$ can be guided by the parameters $r_c$ and $u_{net}^{min}$ specifying the VLP-dendrimer interaction driving the spontaneous assembly of VLPs of different variant types into ordered arrays as observed in experiments near a threshold ionic strength $I_t^{\text{expt}}$. Experiments show that the nearest neighbor spacing $l$ between two P22 VLPs in an ordered array bridged by an interstitial dendrimer is smaller than the VLP-dendrimer-VLP touching distance $(\sigma_v + \sigma_d)$ by $\approx 0.9$ nm on average with a broad variation from $l \approx \sigma_v + \sigma_d$ to $l \approx \sigma_v + \sigma_d - 2.8$ nm[28,29,56]. This points to a strong VLP-dendrimer attraction which translates in our model into an average distance of closest approach $r_c \lesssim r_T$, where $r_T = (\sigma_v + \sigma_d)/2$ is the VLP-dendrimer touch distance. Thus, we constrain $\sigma_{hc}$ values for each variant to those that produce $r_c \lesssim r_T$, as illustrated in Fig. 1(a), where the dashed vertical line represents $r_T$. For all variants, $r_c \lesssim r_T$ for $\sigma_{hc} \in (3.5, 6.5)$ nm. Further, $r_c$ decreases with increasing $\sigma_{hc}$ within this range.

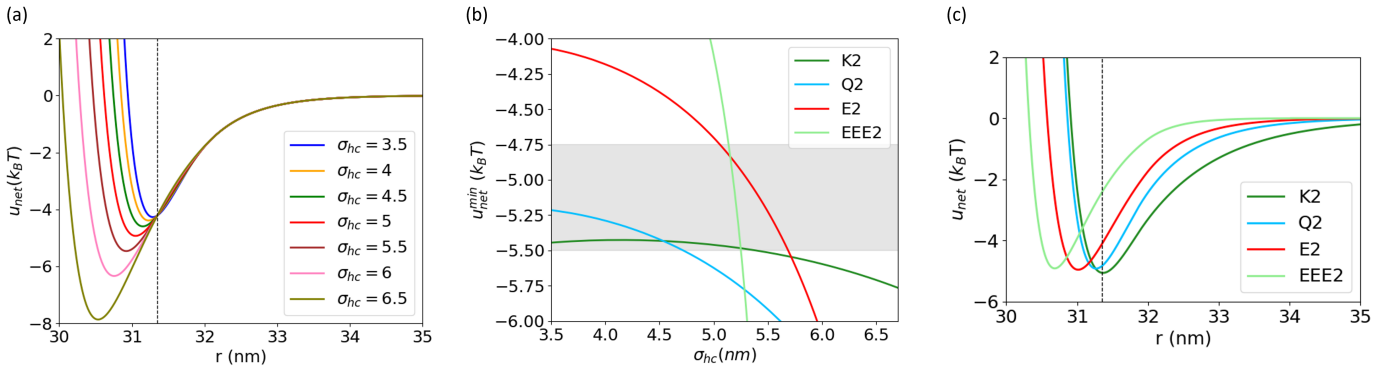


Fig. 1 (a) The net VLP-dendrimer potential $u_{net}(r)$ for a P22-E2 VLP at 240 mM for different proximity parameters $\sigma_{hc}$. (b) Minimum of the net potential $u_{net}^{min}$ vs $\sigma_{hc}$ for different P22 variants near the respective experimentally-observed ionic strength threshold values. The gray region denotes $u_{net}^{min} \in (-4.75\,k_BT, -5.5\,k_BT)$. (c) $u_{net}(r)$ near the threshold values predicted by simulations, using $\sigma_{hc}$ = 4 nm for P22-K2 and P22-Q2 VLPs, and $\sigma_{hc}$ = 5.16 nm for P22-E2 and P22-EEE2 VLPs. Vertical dashed lines in (a) and (c) indicate the VLP-dendrimer touch distance $r_T = 31.5$ nm.

The minimum value of the VLP-dendrimer net potential, $u_{net}^{min}$, associated with the spontaneous assembly of VLPs into ordered arrays sets up another constraint on $\sigma_{hc}$. $u_{net}^{min}$ represents the potential energy gain associated with a dendrimer binding to a VLP. This gain needs to be large enough for dendrimers to be recruited by VLPs and yet sufficiently small for VLPs to avoid over-recruiting dendrimers and aggregating into kinetically-trapped amorphous clusters, as observed in experiments and simulations[29,56]. Through simulations, we observe that the assembly of VLPs of different variants into ordered arrays is associated with $u_{net}^{min}$ between $-4.75\,k_BT$ and $-5.5\,k_BT$.

The above arguments show that $\sigma_{hc}$ values that produce $u_{net}^{min} \in (-4.75\,k_BT, -5.5\,k_BT)$ at $r_c \lesssim r_T$ exhibit a dendrimer-VLP proximity consistent with the observed assembly behavior of different variants near the threshold ionic strengths. We refer to $\sigma_{hc}$ as the proximity parameter. Figure 1(b) shows $u_{net}^{min}$ vs $\sigma_{hc}$ for P22-K2, P22-Q2, P22-E2, and P22-EEE2 variants at $I = 70, 150, 250, 560$ mM respectively. These $I$ values are near the respective $I_t^{\text{expt}}$ associated with each variant. $\sigma_{hc}$ values that produce $u_{net}^{min} \in (-4.75\,k_BT, -5.5\,k_BT)$ are different for different variants. For example, a wide range of $\sigma_{hc}$ constrains $u_{net}^{min} \in (-4.75\,k_BT, -5.5\,k_BT)$ for P22-K2, however, only a very narrow range of $\sigma_{hc}$ values yields the appropriate $u_{net}^{min}$ for the highest-charged variant P22-EEE2.

The above analysis points out the need to relax the restriction of fixing $\sigma_{hc}$ to a single value across all variants, as was the case with our earlier models[29,56], to enable the study of systems comprising variants with a wide range of surface charge. Based on Fig. 1(b), we choose $\sigma_{hc} = 4$ nm for P22-K2 and P22-Q2 variants, and a higher $\sigma_{hc} = 5.16$ nm for P22-E2 and P22-EEE2 variants. These choices produce $r_c \lesssim r_T$ and similar $u_{net}^{min}$ values within the $(-4.75\,k_BT, -5.5\,k_BT)$ range for all variants at $I \sim I_t^{\text{expt}}$. Figure 1(c) shows the net VLP-dendrimer potential $u_{net}(r)$ associated with the four variants at their respective $I_t^{\text{sim}}$. $r_c$ changes with the variant, ranging from $\approx r_T$ to $r_T - 0.6$ nm, and $u_{net}^{min}$ is nearly the same ($\approx -4.85\,k_BT$) across all variants.

There exists a certain degree of freedom, as illustrated by Fig. 1(b), in selecting the proximity parameters characterizing the variants. Similar variability has been noted previously[29] in the choices for effective surface charges of VLP variants and dendrimers. The VLP assembly behavior can be captured using coarse-grained models characterized with small variations in these parameters as long as they produce a dendrimer recruitment energy drive characterized by $u_{net}^{min} \sim -5k_BT$ at $r_c \lesssim r_T$ near $I_t^{\text{expt}}$. We attribute this "model elasticity" to the inevitable limitations of our coarse-grained approach that makes a number of approximations in deriving a minimal representation of a complex system comprising many distinct components including VLPs, dendrimers, salt ions, and solvent molecules. For example, condensation of counterions on VLPs and dendrimers can vary with changes in salt concentration, which can alter the effective charge of VLPs and dendrimers. Our model also ignores the dendritic (branched) structure of dendrimers[65,66], which can affect the dendrimer-VLP steric interaction, particularly as the dendrimers get pulled closer to the VLP surface. Similarly, the flexibility of polymeric chains forming the dendrimers can make them conform to the VLP surface, enabling them to approach closer to the VLP surface, particularly when dendrimers are bridging a pair of VLPs. Accounting for this "squishy" nature of dendrimers via a single adjustable parameter (the proximity parameter $\sigma_{hc}$) is a simplified picture, and a finer-grained model description will be needed to more comprehensively capture the dendrimer flexibility and branching effects on their bridging behavior.

### 2.3 Simulation details

Simulations were performed in an NVT ensemble using the LAMMPS[67] MD package. Initial states comprising 540 VLPs and 54000 dendrimers for 1- and 2-component systems, and 1500 VLPs and 150000 dendrimers for 3- and 4-component systems, were generated in a periodic unit cell with cubic geometry. For mixtures of many types of VLPs, the total number of VLPs was divided equally between variants to achieve equimolar stoichiometry.

Positions and velocities of particles were updated using the velocity Verlet algorithm with a timestep $\Delta t \approx 4$ ps. A Nosé-Hoover thermostat with a damping timescale parameter set to $100\Delta t$ was used to maintain the temperature at $T = 298$ K. Screened electrostatic interactions were cutoff at a distance where the net poten-

tial dropped below $0.005k_BT$. This cutoff distance changed with salt concentration and the variant charge. A typical simulation for a 4-component mixture ran for $\approx 1$ milliseconds and took $\approx 200$ hours to complete on 32 cores using MPI parallelization method. Simulations producing VLP aggregates required longer time to reach a steady-state and were run sufficiently long to obtain converged results.

At periodic intervals during the simulation, the positions of VLPs and dendrimers were stored to compute structural quantities such as pair correlation functions and VLP-bound dendrimer statistics. VLP positions were stored every $10^4$ steps, and a complete set of VLP and dendrimer positions was recorded every $10^5$ steps. These post-processing calculations were performed using a combination of code written in C++ and Python. VLP-VLP pair correlation functions converged using a bin width of $\delta r = 0.005\sigma_v = 0.28$ nm, where $\sigma_v$ is the VLP diameter. To evaluate VLP-bound dendrimer statistics, a nearest neighbor algorithm with a fixed-distance cutoff of $1.05r_T$ was used[29,68].

All VLP-dendrimer systems, including mixtures of many P22 variants, were prepared at an overall VLP concentration of $c_v = 370$ nM, which is $10\times$ higher than the experimental value, and the same bulk dendrimer concentration of $c_d = 37$ $\mu$M as in experiments. In agreement with our previous studies[29,56], simulations at experimental conditions of $c_v = 37$ nM and $c_d = 1000c_v = 37$ $\mu$M produced an assembly behavior similar to that observed in simulations at $c_v = 370$ nM and $c_d = 100c_v = 37$ $\mu$M, with comparable threshold ionic strengths and structural features associated with the assembly products. The lower computational costs of simulations at $c_v = 370$ nM and $c_d = 100c_v$ enabled us to explore a variety of VLP-dendrimer systems including multicomponent mixtures over a wide range of solution conditions.

MD simulations were performed with two separate modes of electrostatic control to bring the NP-linker system at a target ionic strength $I$: dialysis and rapid dilution. For dialysis, starting from a system equilibrated at a high ionic strength $I_h$, where the solution exhibited a liquid-like behavior, $I$ was decreased gradually in a stepwise fashion, allowing for equilibration between each step. In the case of rapid dilution, the system was prepared at $I_h$ and the ionic strength was quickly lowered (in a single step) to the target $I$, where the system was allowed to equilibrate.

## 3 Results and Discussion

Results for one-component systems are discussed first, followed by a discussion on the results for the multicomponent mixtures of two, three, and four variants. The last subsection elucidates the link between the VLP assembly products and the VLP-bound dendrimer statistics. Results for systems that include the P22-EEE2 variant, which remained inaccessible with previous models, are highlighted and their comparison with experiments are noted.

### 3.1 One-component systems

The assembly behavior of one-component systems comprising VLPs associated with only one variant type in the presence of dendrimers was studied for ionic strengths modulated via the rapid dilution approach. Figure 2a shows the assembly products of P22-EEE2 VLPs through representative simulation snapshots at selected $I$ values: $560, 550, 400, 200, 100$ mM. For $I > 550$ mM, the VLPs remained in a liquid-like state as illustrated for the case of $I = 560$ mM. A decrease in $I$ to 550 mM showed a dramatic change with VLPs aggregating to form ordered arrays. The VLP-VLP pair correlation function (PCF) $g(r)$ shown in Figure 2b confirmed these observations. At $I = 560$ mM, $g(r)$ exhibited a single peak corresponding to weak interactions between VLPs at short distances, however, at $I = 550$ mM, $g(r)$ showed multiple sharp peaks at positions consistent with an FCC/HCP lattice structure, indicative of longer-range order.

The ionic strength at which the system exhibits ordered aggregates and above which no significant assembly occurs, defined as the ionic strength threshold $I_t^{\text{sim}}$, was found to be in good agreement with experiments on EEE2 VLPs (Table 1). For $I < I_t^{\text{sim}}$, VLPs continued to assemble into aggregates albeit with progressively diminished order with decreasing $I$. For example, at $I = 400$ mM, aggregates are observed, however, the peaks in the corresponding $g(r)$ are much less pronounced. Lowering the ionic strength to $I = 200$ mM enhances the disappearance and attenuation of these $g(r)$ peaks. For $I \lesssim 100$ mM, the snapshots and PCF show that VLPs remain either dispersed in the solution or form very small clusters comprising a few VLPs. These findings are consistent with experimental results reported in previous studies[29,56].

In addition to capturing the previously inaccessible assembly behavior of the P22-EEE2 variant, the new coarse-grained model reproduced the assembly behavior observed in past simulations and experiments of the smaller-charge variants: P22-E2, P22-Q2, and P22-K2[29]. The Supplementary Information (SI) provides the simulation snapshots and PCFs (Figures S1, S2, and S3). The ionic strength thresholds $I_t^{\text{sim}}$ predicted by simulations for these variants were found to be in good agreement with the corresponding experimental $I_t^{\text{expt}}$ values (Table 1). The threshold decreased with decreasing charge of the VLPs, i.e., $I_t^{\text{EEE2}} > I_t^{\text{E2}} > I_t^{\text{Q2}} > I_t^{\text{K2}}$.

Increasing the ionic strength above the ionic strength threshold associated with a variant weakens the electrostatic VLP-dendrimer attraction compared to the entropic gain accessible to either particle by remaining dispersed in the solution. In general, the threshold value is determined by the charge and size of VLPs and dendrimers as well as the proximity parameter modulating the extent to which the dendrimers may approach the VLPs. An approximate relation to estimate the threshold ionic strength $I_t$ for a given variant to form ordered arrays can be derived by noting that this assembly is driven by a net VLP-dendrimer attraction $u_{net}(r)$ that enables an optimal recruitment of dendrimers to act as bridges between the VLPs. Using Equations 1 and 3, we obtain the relation $u_{net}(r_c) = u_{net}^{min}$, where $u_{net}^{min} \approx -5k_BT$ is the optimal potential energy gain associated with a dendrimer-VLP bond, and $r_c = r_T - h$ is the dendrimer-VLP distance of closest approach, with $r_T$ being the dendrimer-VLP touch distance and $h$ denoting the extent of overlap between a dendrimer and a VLP. We introduce the dimensionless dendrimer-VLP Coulomb energy $U_C = |l_B q_v q_d / r_T|$ as a parameter to quantify the strength of the dendrimer-VLP attraction. In general, experiments show that $h$ can change with the variant[28,29,56]. To simplify the analysis, informed by the $u_{net}(r)$ profiles for different variants near $I_t^{\text{sim}}$ (Figure 1(b)), we assume

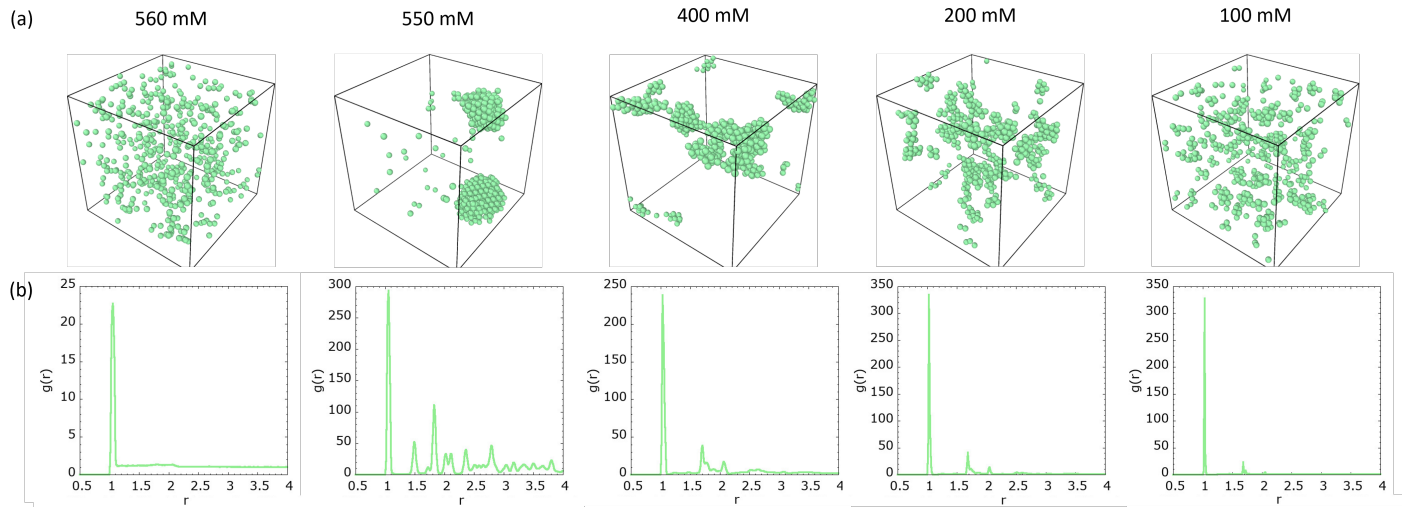


Fig. 2 (a) Assembly of P22-EEE2 VLPs (green spheres) mediated by G6 dendrimers (not shown for clarity) via rapid dilution starting from 600 mM to selected ionic strengths $I$ indicated by the legend at the top of the snapshots. Snapshots show fluid-like behavior for $I$ higher than the threshold $I_t = 550$ mM, the emergence of long-range order at $I \sim I_t$, and the formation of increasingly less-ordered structures with decreasing $I$ for $I < I_t$. Note that the clusters seen at $I \sim I_t$ are part of a larger ordered array considering the periodic boundary conditions used in the simulation. (b) Pair correlation functions characterizing the assembly products formed at the selected ionic strengths.

$h \approx 0$ for the lower-charged P22 variants (e.g., K2 and Q2) defined by $U_C < U_C^*$, where for our case we approximate $U_C^* = 1200$, and $h \approx 0.5$ nm for the higher-charged variants (e.g., E2 and EEE2) characterized with $U_C > U_C^*$.

With these simplifications and noting that $\kappa\sigma_v \gg 1$, the relation $u_{net}(r_c) = u_{net}^{min}$ transforms into the equality: $U_C e^{\kappa h} - B(1+\sigma_d\kappa/2)\,\sigma_v\kappa/2 = 0$, where $B(\sigma_{hc}, h) = u_{mLJ}(r_T - h) - u_{net}^{min}$ is in units of $k_BT$ and depends on the proximity parameter $\sigma_{hc}$, the overlap distance $h$, and the net energy gain $u_{net}^{min}$ associated with a dendrimer-VLP bond. For the lower-charged variants, this equation simplifies using $h \approx 0$ and $B \approx 6$, yielding an analytical estimate for the screening parameter (in nm$^{-1}$) $\kappa \approx (1/\sigma_d)(\sqrt{1+4(U_C/6)(\sigma_d/\sigma_v)} - 1)$ and the threshold ionic strength $I_t \approx 0.09\kappa^2$ (in M). Note that $I_t$ depends on the charge and size parameters of the variant and linker, but does not depend on the proximity parameter, which is consistent with the observation that a wide range of $\sigma_{hc}$ values are able to produce the optimal $u_{net}^{min}$ and $r_c \sim r_T$ for the lower-charged variants. For the specific case of P22 VLPs and G6 PAMAM dendrimers, we find $I_t$ scales almost linearly with increasing $U_C$ within $U_C \in (400, 1200)$. The analytical result yields $I_t$ estimates of $\approx 0.07$ and $\approx 0.15$ M for the K2 and Q2 variants respectively, which are in good agreement with simulation and experimental findings.

For the higher-charged variants characterized with $U_C > U_C^*$ and $h \approx 0.5$ nm, the exponential term in the aforementioned equality cannot be neglected and $B$ depends explicitly on the proximity parameter. Setting $\sigma_{hc} = 5.16$ nm for the higher-charged variants, we obtain $B \approx 12$, which yields a transcendental equation for $\kappa$: $U_C e^{\kappa/2} - 12(1+\sigma_d\kappa/2)\,\sigma_v\kappa/2 = 0$. This equation can be solved numerically to yield estimates for $I_t$ via $I_t \approx 0.09\kappa^2$ (in M). For our specific case of P22 VLPs and G6 dendrimers, $I_t$ exhibits a faster than linear rise with increasing $U_C$ in the range $U_C \in (1200, 2500)$, and we find estimates of $\approx 0.23$ and $\approx 0.5$ M for the E2 and EEE2 variants respectively, which are within 10% of the simulation and experimental findings. The closed-form analytical result and the above transcendental equation (which can be readily solved, e.g., using Mathematica) can be used as a rough guide to predict the ionic strength thresholds for charged components with different surface charges and sizes over an approximate range of $U_C \in (400, 2500)$ and $I \in (0.05, 0.6)$ M values.

### 3.2 Two-component mixtures

The model was next applied to study the dendrimer-mediated assembly of mixtures of two types of VLPs. Our previous paper[56] showed that in an equimolar (1 : 1) two-component mixture of E2 and K2 VLPs, the disparity in the ionic strength threshold associated with the two variants can be leveraged via salt dialysis to produce multilayered nanostructures. Dialysis-based modulation of the ionic strength established the electrostatic drive to selectively assemble the E2 VLPs in the mixture into an ordered array (core) by lowering $I$ to $I_t^{E2}$, and subsequently assemble the K2 VLPs into a layer enveloping the E2 core by further decreasing $I$ to $I_t^{K2}$. Here, we examine the generality of this sequential hierarchical assembly strategy by probing two new equimolar two-component systems: a mixture of EEE2 and E2 VLPs, discussed below, and a mixture of E2 and Q2 VLPs, described in the SI. For the sake of completeness, the SI also describes the simulations of the mixture of E2 and K2 VLPs using our new model, which produced results in agreement with our past findings[56].

In the dialysis approach, starting from a solution of EEE2 VLPs, E2 VLPs, and dendrimers equilibrated at 600 mM, the ionic strength was gradually reduced in small steps yielding equilibrated mixtures at $I = 570, 550, 500, 400, 350, 325, 300, 245, 100$, and 40 mM. Figure 3(a) shows the simulation snapshots and PCFs associated with the steady-state assembly products for a subset of the $I$ values. For two-component mixtures, it is useful to examine three types of PCFs: two self PCFs (EEE2-EEE2 PCF, E2-E2 PCF),

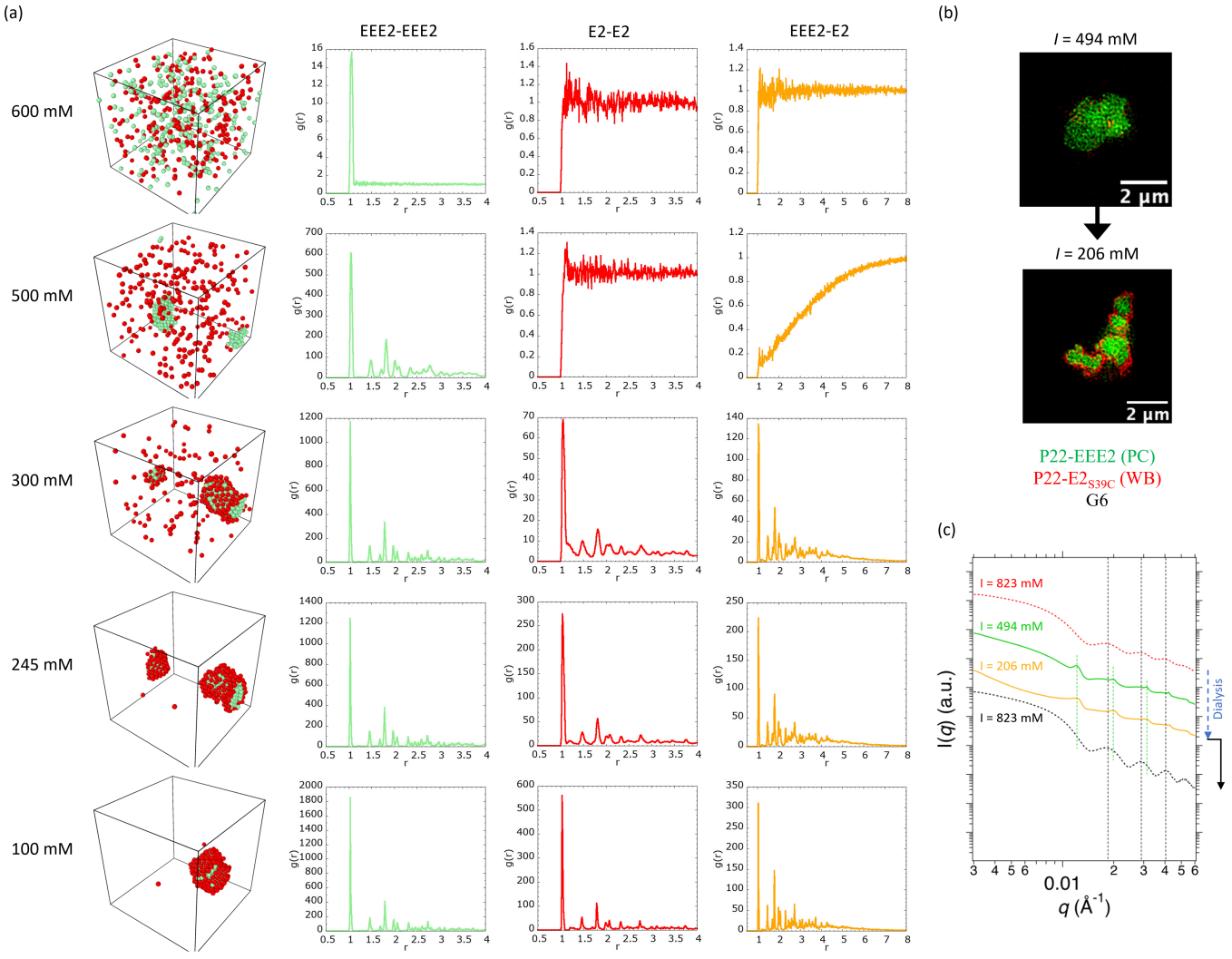


Fig. 3 (a) Representative simulation snapshots of the steady-state assembly products associated with a two-component mixture of P22-EEE2 (green spheres) and P22-E2 VLPs (red spheres) realized via salt dialysis to ionic strengths $I$ indicated on the left. G6 dendrimers are not shown on the snapshots for clarity. The second, third, and fourth columns show the EEE2-EEE2 PCF (green), E2-E2 PCF (red), and EEE2-E2 PCF (orange) respectively. No assembly is observed at $I = 600$ mM (top). Exclusive assembly of P22-EEE2 VLPs occurs at its ionic strength threshold $I_t^{EEE2} =$ 550 mM resulting in an ordered aggregate (second row); the EEE2-E2 PCF shows that the P22-EEE2 VLP core actively excludes P22-E2 VLPs. Co-assembly with a layer of E2 VLPs enveloping the EEE2 VLP core occurs upon further dialysis to $I = 300$ mM (center row) and near the E2 threshold, $I_t^{E2} = 245$ mM. Core-shell structures persist at lower $I$ values (bottom row), with PCF peaks sharpening as $I$ is dialyzed down to 100 mM. (b) Fluorescence microscopy images of EEE2-E2 mixture showing the core and core-shell structures. P22-EEE2 VLPs were labeled with Alexa-488 and P22-E2 VLPs were labeled with Texas Red. (c) Structure factor $I(q)$ observed in SAXS data associated with aggregates at $I = 823, 494, 206$ mM. The sequence of events to change the ionic conditions is displayed with dashed arrows indicating the step-wise dialysis and the solid arrow to show direct buffer replacement to change the ionic strength after isolating the assemblies by gentle centrifugation.

and one cross PCF (EEE2-E2 PCF). At 600 mM, which exceeds the ionic strength threshold of either species, no significant assembly is observed. The PCFs show features characteristic of a simple liquid; the EEE2-EEE2 PCF shows a single peak reflective of transient "dimer" formation while the E2-E2 PCF and EEE2-E2 cross PCF show no semblance of any clear short-range order.

At 500 mM, the higher-charged EEE2 VLPs aggregate while the lower-charged E2 VLPs remain dispersed in the solution. The self EEE2-EEE2 PCF at $I = 500$ mM indicates that the aggregate formed by the EEE2 VLPs is ordered, similar to the arrays observed for the single-component P22-EEE2 variant system in Figure 2(a). The cross EEE2-E2 PCF shows that the ordered array ("core") excludes E2 VLPs. Dialyzing down to $I = 300$ mM produces a layer ("shell") of E2 VLPs around the EEE2 VLP core. The layering is nearly complete as $I$ approaches $I_t^{E2} = 245$ mM, the ionic strength threshold associated with the E2 variant. Core-shell structures persist below $I_t^{E2}$ with PCF peaks sharpening at $I = 100$ mM. The associated EEE2-EEE2 and E2-E2 PCFs show that a similar lattice structure is shared by the core and the shell.

These findings closely match the experimental results shown in Figures 3(b) and (c). Fluorescence microscopy images corresponding to $I$ just below $I_t^{EEE2}$ show only the presence of an EEE2 VLP cluster. When $I$ is dialyzed down close to $I_t^{E2}$, the EEE2 cluster (green) is enveloped by a layer of E2 VLPs (red). SAXS data associated with the assembly products at $I = 823, 494, 206$ mM confirm these observations and produce structure factors $I(q)$ consistent with the PCF results.

The slow modulation of the ionic strength via dialysis is critical to the realization of ordered core-shell structures. Figure 4 shows the assembly products associated with the EEE2-E2 mixture produced via rapid dilution at the $I$ values shown in Figure 3 starting from the same fluid-like state at 600 mM. Decreasing $I$ rapidly to 500 mM produces an assembly state similar to the dialysis case where the EEE2 VLPs aggregate into an ordered array while the E2 VLPs remain dispersed. Rapid dilution to $I = 300$ mM, however, yields a very different outcome: EEE2 and E2 VLPs mix together into amorphous aggregates instead of co-assembling into spatially segregated, layered structures based on a "pre-formed" EEE2 core, as realized via dialysis. The amorphous aggregates are characterized with a much lower degree of order compared to the core-shell structures produced with dialysis.

Decreasing $I$ rapidly to $I_t^{E2} = 245$ mM generates similar kinetically-trapped structures exhibiting a mixed composition of EEE2 and E2 VLPs. As part of a single-component system, E2 VLPs produced ordered arrays via rapid dilution to 245 mM (Figure S3) while EEE2 VLPs assembled into amorphous aggregates with reduced order (Figure 2). This proclivity of EEE2 VLPs to form kinetically-trapped clusters disrupts the assembly pathways of E2 VLPs to form ordered arrays near $I_t^{E2}$ in the two-component mixture. Rapid dilution to $I \ll I_t^{E2}$ produces increasingly small co-aggregates characterized with an overall reduced order.

The same general assembly behavior is observed across all probed two-component mixtures, for both the dialysis and rapid dilution approaches (Supplemental Figures S4-S7), and the results closely match experimental observations[56]. Gradual or rapid reduction in the ionic strength to values near the ionic strength threshold for the higher-charged variant produces the same outcome: the higher-charged VLPs aggregate into ordered arrays, while the lower-charged VLPs remain dispersed. Dialyzing the ionic strength close to the ionic strength threshold of the lower-charged variant leads to the formation of a core composed of the higher-charged VLPs, and an outer shell composed of the lower-charged VLPs, whereas rapid dilution yields aggregates with a mixed composition of both types of VLPs.

An interesting feature of the two-component systems is that, regardless of dialysis or rapid dilution, the higher-charged VLPs alter the assembly behavior of the smaller-charged VLPs *above* their ionic strength threshold $I_t$ established via the examination of the one-component assembly behavior. For example, E2 VLPs in the two-component EEE2-E2 mixture at $I = 300$ mM organize into an ordered layer enveloping the EEE2 core using dialysis (Figure 3) or mix with the EEE2 VLPs to form amorphous aggregates via rapid dilution (Figure 4). However, as part of a single-component system, E2 VLPs do not exhibit any aggregation at $I = 300$ mM, and remain dispersed in a liquid-like state (Figure S3). These findings are consistent with our previous study on the two-component E2-K2 system where both simulations and experiments showed that in the case of dialysis, the lower-charged K2 VLPs organize into a layer around the E2 core above $I_t^{K2}$ [56]. Simulations of the E2-K2 system with the new model reproduce these results (Figures S4 and S5). As elucidated in detail in Sec. 3.5, the change in the assembly behavior of the lower-charged VLPs at $I > I_t$ can be attributed to the enhanced dendrimer recruitment potential of these VLPs resulting from the presence of the dendrimers bound to the surface of the higher-charged VLPs.

The ionic strength $I > I_t$ up to which the behavior of the lower-charged variant is affected by the presence of the higher-charged variant depends on the specific mixture. We illustrate this effect for the EEE2-E2 mixture in Figure 5 by showing the dialysis results at a higher granularity of ionic strengths $I \in [300, 500]$ mM. A layer of E2 VLPs continues to envelop the EEE2 VLP core at $I = 325$ mM; the associated PCFs reveal the presence of long-range order. At $I = 350$ mM, while no E2 layer is observed around the EEE2 core, the EEE2-E2 PCF reveals a clear correlation between the two types of VLPs. Strikingly, the E2-E2 PCF shows first and second peaks, in contrast with the no-assembly state observed at $I > I_t^{E2}$ in a one-component E2 system. Only when $I$ is increased to 400 mM, all order is lost and the associated PCFs appear similar to the liquid-like state observed at 500 mM.

These results taken together with those obtained with rapid dilution, which show similar trends, reveal that EEE2 VLPs alter the pathways associated with the assembly of E2 VLPs up to $\approx 100$ mM higher than the threshold $I_t^{E2}$ for the E2 variant. Similarly, examining the assembly behavior of E2-Q2 and E2-K2 mixtures (Figures S4-S7 in the SI) shows the influence of higher-charged VLPs lasts up to 40 mM and 55 mM, respectively, above the respective threshold values $I_t^{Q2}$ and $I_t^{K2}$ of the lower-charged VLPs.

### 3.3 Three-component mixtures

The model was next used to study the assembly behavior of equimolar (1 : 1 : 1) mixtures of 3 types of P22 variants in the

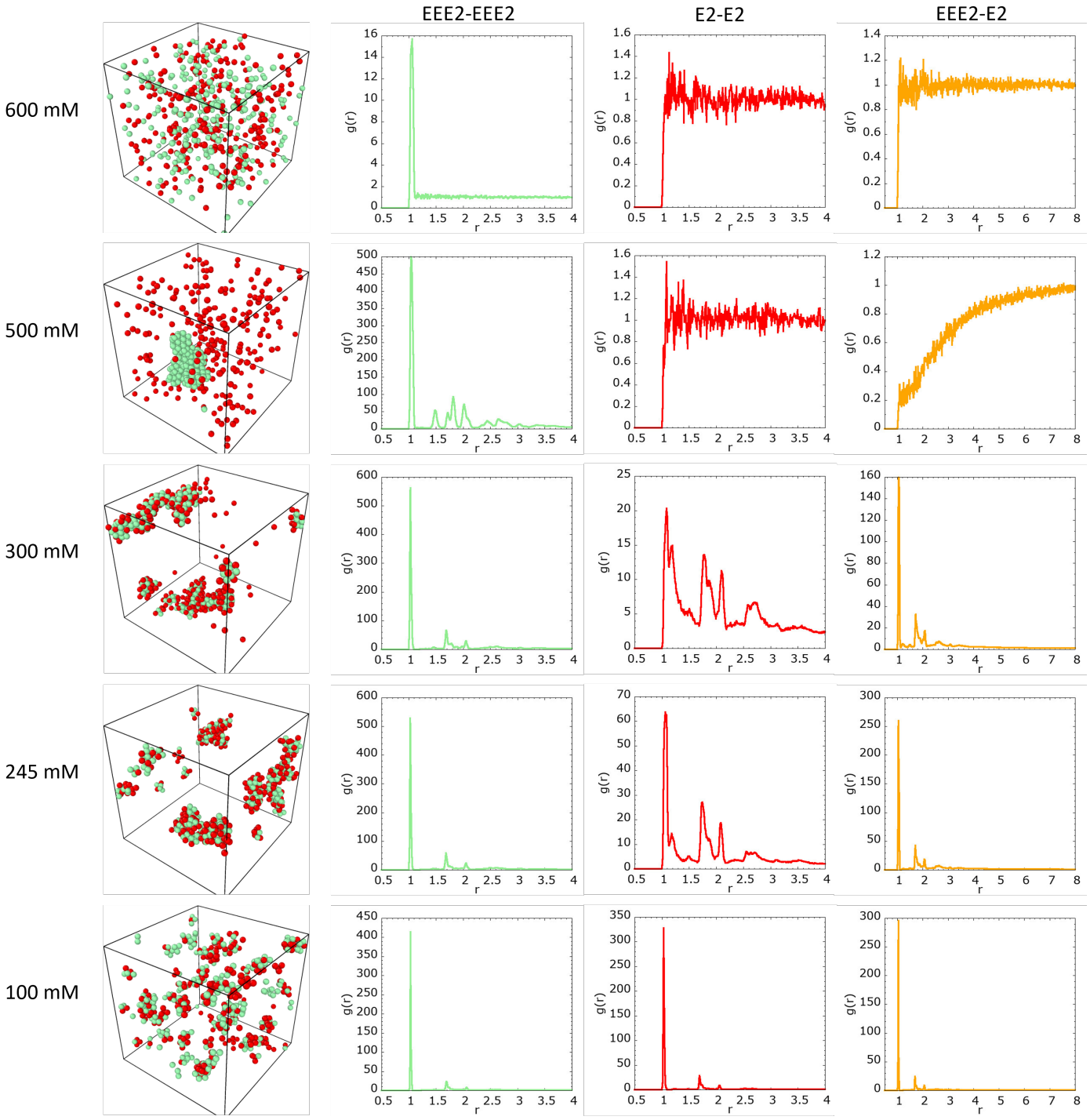


Fig. 4 Representative simulation snapshots of the steady-state assembly products associated with a two-component mixture of P22-EEE2 (green spheres) and P22-E2 VLPs (red spheres) realized via rapid dilution at ionic strengths indicated on the left. G6 dendrimers are not shown for clarity. The second, third, and fourth columns show the EEE2-EEE2 PCF (green), E2-E2 PCF (red), and EEE2-E2 PCF (orange) respectively.

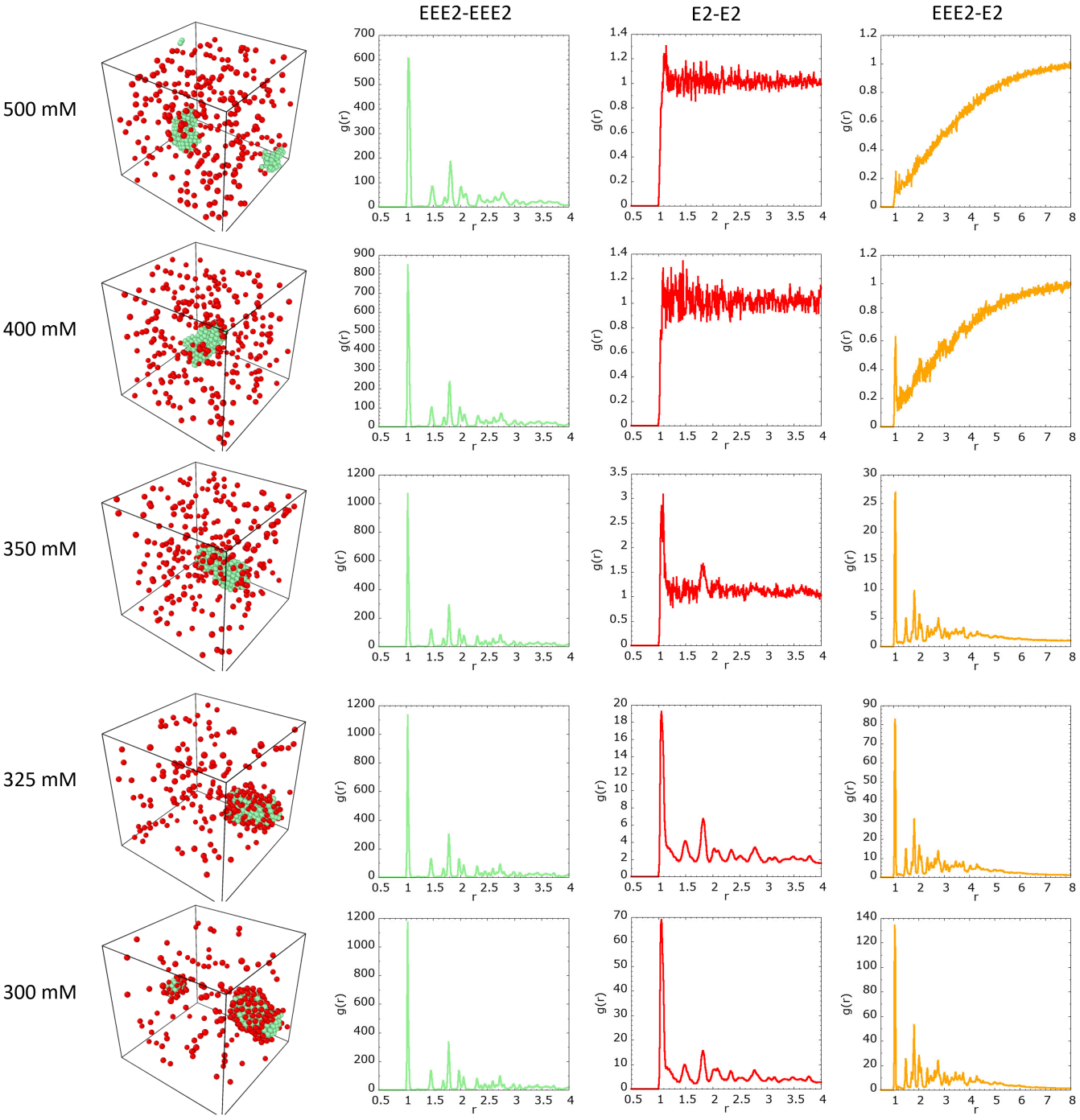


Fig. 5 Assembly products of a two-component mixture of P22-EEE2 and P22-E2 VLPs realized via dialysis for ionic strengths between 300 and 500 mM indicated on the left. Left column shows the representative simulation snapshots; G6 dendrimers are not shown for clarity. The second, third, and fourth columns show the EEE2-EEE2, E2-E2, EEE2-E2 PCFs respectively. Emergence of order is evident even at 350 mM despite the ionic strength threshold for assembly of E2-only one-component system being $\approx 250$ mM.

presence of oppositely charged dendrimers. The total viral concentration was maintained at $c_v = 370$ nM, and the dendrimer concentration was set to $c_d = 100c_v$. Two different mixture compositions were studied using dialysis and rapid dilution methods: a mixture of EEE2, E2 and Q2 VLPs (discussed below), and a mixture of E2, Q2, and K2 VLPs (discussed in the SI).

In the dialysis approach, starting from a state equilibrated at 600 mM, $I$ was decreased gradually in small steps to yield equilibrated mixtures at $I = 500, 400, 350, 325, 300, 245, 200, 160, 100, 75, 40$ mM. Figure 6 shows the representative simulation snapshots characterizing the assembly states of the EEE2-E2-Q2 mixture produced via dialysis for a subset of these values: $I = 600, 500, 400, 350, 300, 245, 200, 160, 40$ mM. Figure 7 shows the associated PCFs (results for $I = 600, 400$ mM are excluded for the sake of clarity.) For a three-component system, a total of 6 PCFs: three self PCFs and three cross PCFs, become relevant in quantitatively assessing the assembly behavior. For $I = 600$ mM, which is higher than the ionic strength threshold values of all variants, a liquid-like state is observed with VLPs of all types dispersed in the solution. For $I = 500, 400$ mM, which are values near the ionic strength threshold $I_t^{EEE2} = 550$ mM of the highest-charged variant, an exclusive assembly of P22-EEE2 VLPs into ordered arrays is observed. The P22-E2 and P22-Q2 VLPs remain in suspension, excluded by the EEE2 aggregates as evident by the EEE2-E2 and EEE2-Q2 cross PCFs.

Dialyzing down to $I = 350$ mM enhances the order associated with the EEE2 aggregates and produces a dramatic shift in the EEE2-E2 cross PCF, signaling the emergence of significant correlation between the EEE2 and E2 VLPs. Dialysis to $I = 300$ mM further enhances these correlations and a layer composed exclusively of E2 VLPs begins to form around the EEE2 aggregates. The E2-E2 PCF shows that the layer exhibits order. The Q2 VLPs continue to remain dispersed in the solution excluded from these "core-shell" structures, and exhibit no significant correlation between each other or with VLPs of other variant types. Decreasing $I$ to the ionic strength threshold $I_t^{E2} \sim 245$ mM of the E2 variant results in the near completion of the E2 layers around the EEE2 cores. The E2-E2 PCF shows an increase in the order associated with these layers. Interestingly, there is a significant change in the EEE2-Q2 cross PCF which shows a clear peak at a distance $r \approx \sigma_v$, indicating strong correlations between the EEE2 VLPs present in the outermost part (surface) of the core and Q2 VLPs. This implies that Q2 VLPs compete with the E2 VLPs for potential recruitment by the EEE2 core. At the same time, the E2-Q2 cross PCF also shows a clear first peak at $r \approx \sigma_v$, signaling the potential for Q2 VLPs to be recruited by the E2 layer itself.

The correlations between Q2 and EEE2 VLPs and those between Q2 and E2 VLPs are enhanced, by a similar degree, upon dialysis to $I = 200$ mM. Thus, Q2 VLPs continue to have similar potential of recruitment by either the EEE2 core or the E2 layer enveloping this core. The Q2-Q2 PCF shows a low degree of short-range order which can be attributed to the organization of Q2 VLPs into small weakly-correlated clusters driven by their proximity to the EEE2-E2 core-shell structures.

The recruitment of Q2 VLPs by the E2 layer is favored when the solution is dialyzed down to the ionic strength threshold $I_t^{Q2} = 160$ mM of the Q2 variant as evidenced by the stronger E2-Q2 cross correlations compared to the EEE2-Q2 correlations. Nearly-complete Q2 layers are observed enveloping the E2 layers formed around the EEE2 cores. The Q2-Q2 PCF shows that these Q2 layers are ordered. Further reduction in $I$ to 40 mM enhances this order and strengthens the cross correlation between Q2 and E2 VLPs, resulting in multilayered ordered arrays.

The SI provides a discussion of the assembly products associated with the EEE2-E2-Q2 mixture when the $I$ values shown in Fig. 6 are reached using rapid dilution starting from the same fluid-like state at 600 mM. Figures S8 and S9 show the snapshots and the associated PCFs respectively.

The same general assembly behavior is observed for the E2-Q2-K2 mixture, for both the dialysis and rapid dilution approaches (Figs. S10-S13). Overall, the findings with three-component mixtures are consistent with the results obtained for two-component systems. Regardless of rapid or gradual dilution, as the ionic strength is decreased to the ionic strength threshold of the highest-charged variant, an ordered core composed exclusively of VLPs of that variant type is formed, while the VLPs of other variant types remain dispersed. Decreasing the ionic strength further via dialysis leads to the formation of layers around the core, with each layer comprising VLPs of a single variant type. The layers are arranged outwards from the core in order of decreasing variant charge. On the other hand, if the ionic strength is decreased via rapid dilution, the formation of multilayered core-shell structures is prevented, and instead, kinetically-trapped aggregates with a mixed composition of VLPs of different variant types are formed.

Similar to the two-component mixtures, the higher-charged VLPs in the three-component mixtures alter the assembly pathways of the lower-charged VLPs *above* their ionic strength threshold $I_t$ established via the examination of one-component assembly states. For example, Q2 VLPs in the EEE2-E2-Q2 mixture at $I = 200$ mM begin organizing in the vicinity of the EEE2-E2 core-shell aggregates into a layer exhibiting weak order (dialysis) or they mix with EEE2 and E2 VLPs to form amorphous aggregates (rapid dilution). However, as part of a single-component system, Q2 VLPs remain dispersed in a liquid-like state, exhibiting no aggregation, at 200 mM (Fig. S2).

### 3.4 Four-component mixtures

We now discuss the results of using the model to probe the assembly behavior of equimolar four-component mixture of EEE2, E2, Q2, and K2 VLPs. The total VLP and dendrimer concentrations were kept the same: $c_v = 370$ nM, $c_d = 100c_v$, and the assembly behavior was explored using dialysis and rapid dilution.

In the dialysis approach, starting from a state equilibrated at 600 mM, the ionic strength $I$ was decreased gradually in small steps to yield equilibrated mixtures at $I = 500, 400, 350, 325, 300, 245, 200, 160, 125, 100, 75,$ and 40 mM. Figure 8 shows the representative simulation snapshots characterizing the steady-state assembly products associated with the EEE2-E2-Q2-K2 mixture for a subset of these values. Figures 9 and 10 show the associated PCFs (results for $I = 600, 400$ mM are ex-

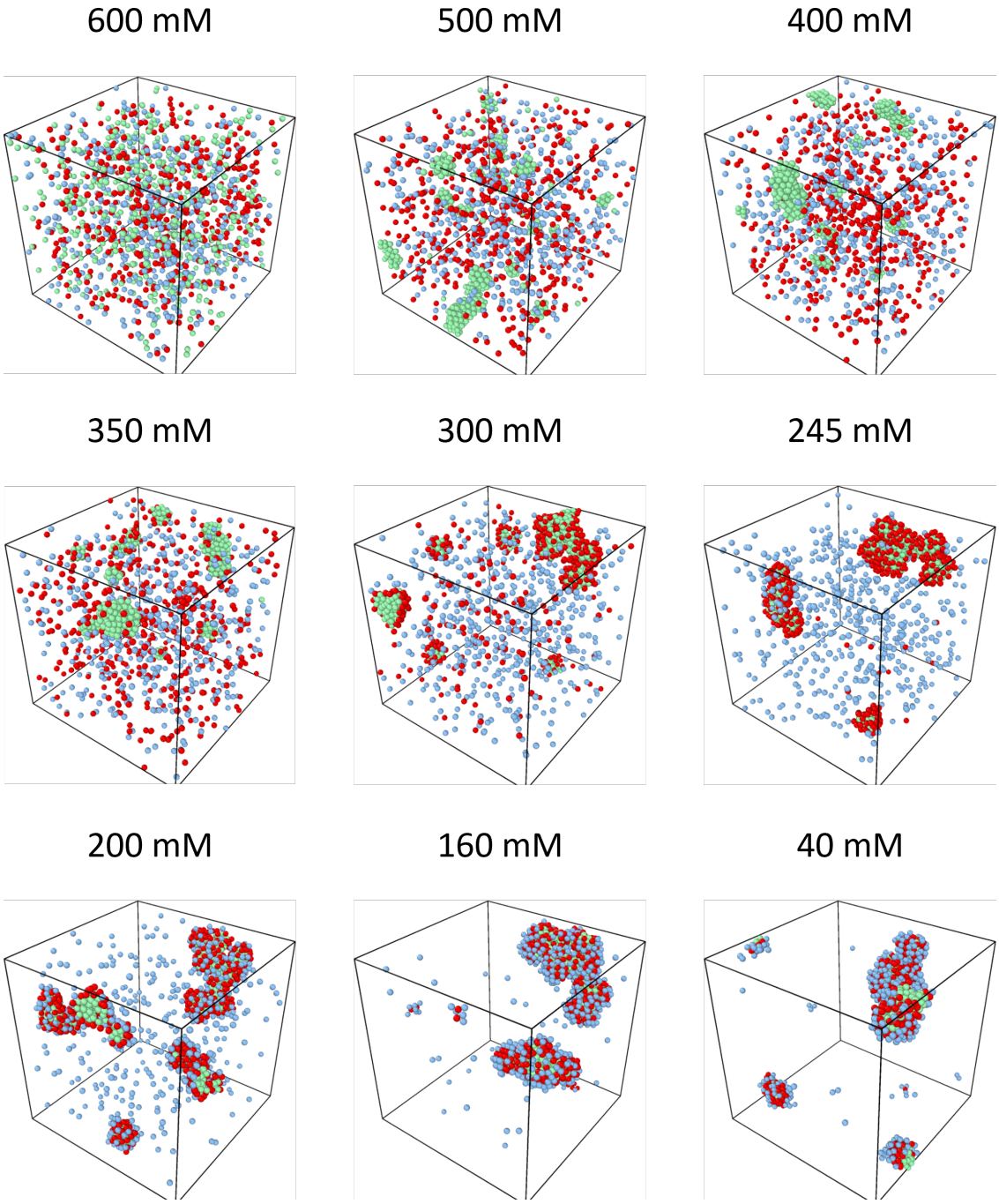


Fig. 6 Representative simulation snapshots of the steady-state assembly products associated with a three-component mixture of P22-EEE2 (green), P22-E2 VLPs (red), and P22-Q2 VLPs (blue) realized via dialysis for the ionic strengths indicated at the top. G6 dendrimers are not shown for clarity.

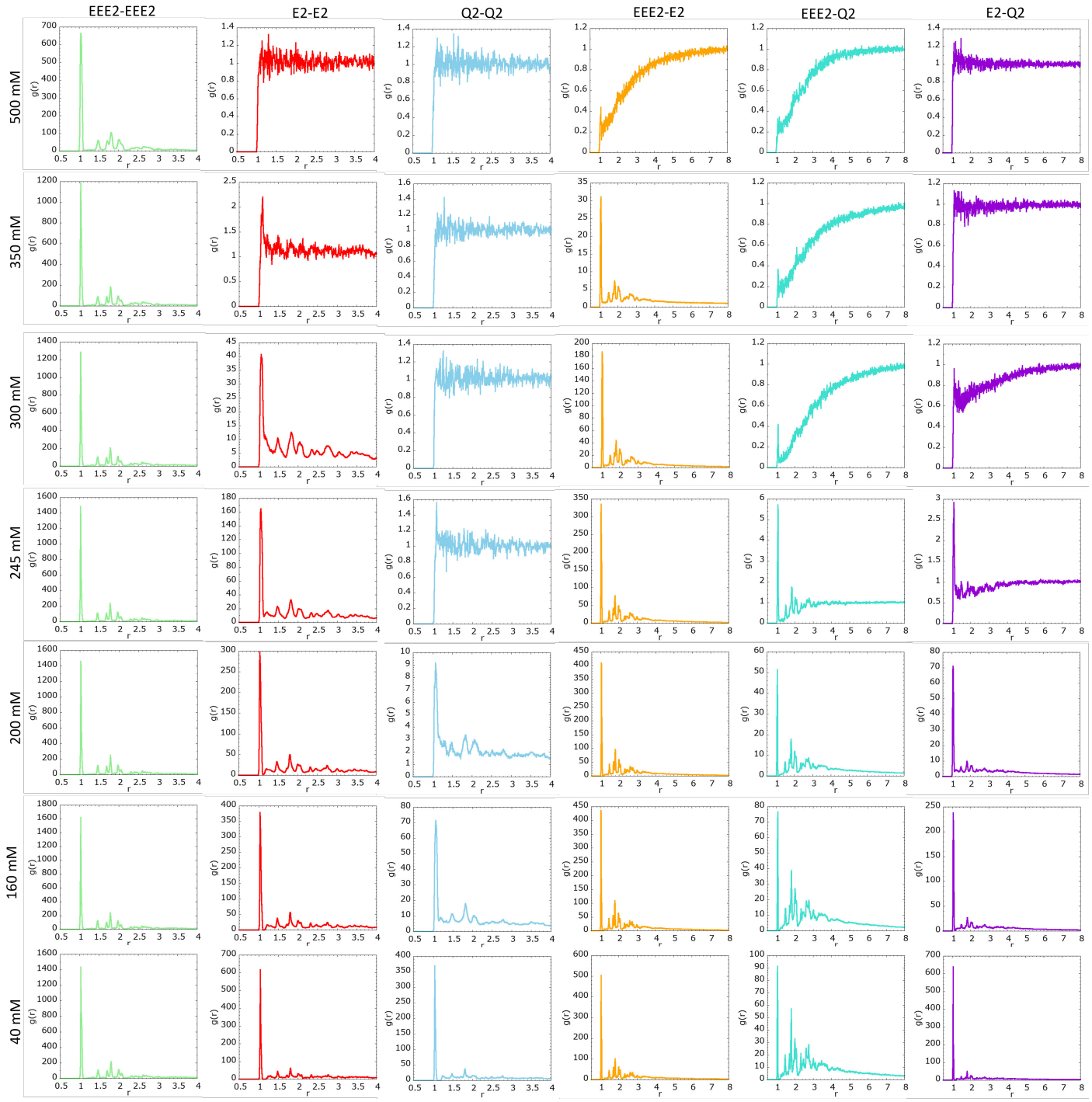


Fig. 7 Pair correlation functions (PCFs) characterizing the assembly products generated via salt dialysis of a three-component mixture of P22-EEE2, P22-E2, and P22-Q2 VLPs in the presence of oppositely charged dendrimers at selected ionic strengths shown on the left. The first, second, and third columns show the self EEE2-EEE2 (green), E2-E2 (red), and Q2-Q2 PCFs (blue) respectively. The fourth, fifth, and sixth columns show the cross EEE2-E2 (orange), EEE2-Q2 (cyan), and E2-Q2 (purple) PCFs respectively.

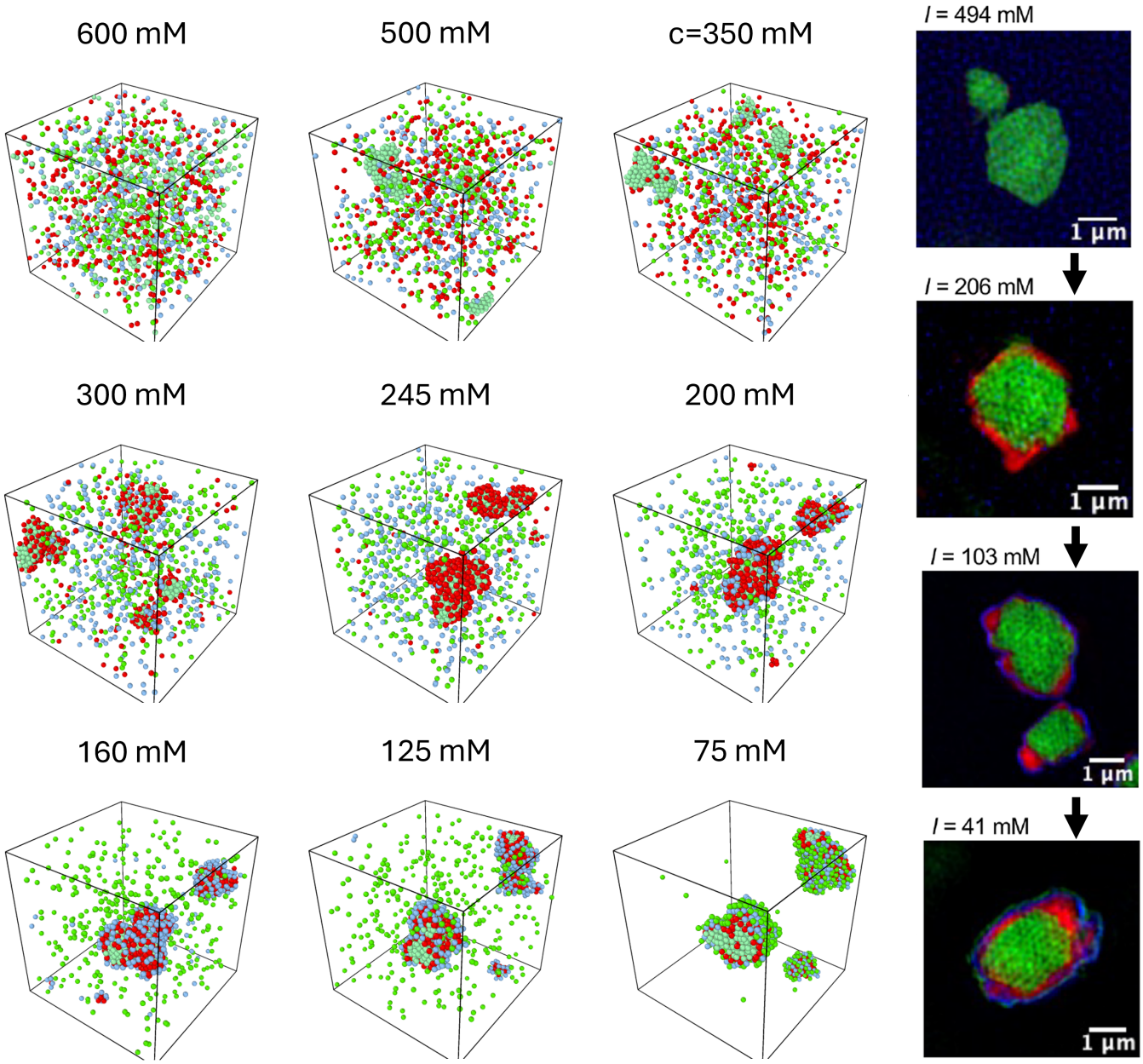


Fig. 8 Representative simulation snapshots of the steady-state assembly products associated with a four-component mixture of P22-EEE2 (green), P22-E2 (red), P22-Q2 (blue), and P22-K2 (bright green) VLPs realized via dialysis for the indicated ionic strengths $I$. G6 dendrimers are not shown for clarity. (Right) Super-resolution fluorescence microscopy images of structures formed in the same mixture using dialysis at the noted $I$ values. P22-EEE2, P22-E2, P22-Q2, and P22-K2 VLPs are labeled with Alexa-488, Texas Red, CF405M, and Alexa-488 respectively (adapted from [56]).

cluded for the sake of clarity.) For a four-component system, ten PCFs: four self PCFs and six cross PCFs, become relevant to quantitatively characterize the assembly products.

A liquid-like state with VLPs of all four variants dispersed in the solution is observed at $I = 600$ mM, which is higher than the $I_t$ of all four variants. Decreasing $I$ to 500 mM, which is below $I_t^{EEE2} = 550$ mM, produces an exclusive assembly of P22-EEE2 VLPs into ordered aggregates. VLPs of the other variant types remain dispersed in suspension excluded from the EEE2 aggregates, as evidenced by the EEE2-E2, EEE2-Q2, and EEE2-K2 cross PCFs. Dialyzing down to 350 mM produces a dramatic shift in the EEE2-E2 cross PCF, signaling the emergence of strong correlations between the EEE2 and E2 VLPs. A layer composed exclusively of E2 VLPs starts forming around the EEE2 cores starting at $\sim 300$ mM. The layer formation is nearly complete by $I \sim I_t^{E2} = 245$ mM, resulting in the generation of ordered EEE2-E2 core-shell structures. Further, a decrease from 300 mM to 245 mM produces a significant change in the EEE2-Q2 and E2-Q2 cross PCFs (e.g., the emergence of a prominent first peak at a distance $r \approx \sigma_v$), which can be attributed to the onset of cross-correlations between Q2 VLPs and the VLPs associated with the EEE2 and E2 variant types.

At $I = 200$ mM, the similarities between the EEE2-Q2 and E2-Q2 cross PCFs indicate that Q2 VLPs are actively recruited by both the exposed regions of the EEE2 core and the E2 layer enveloping the EEE2 core. As $I$ is dialyzed down to the ionic strength threshold $I_t^{Q2} = 160$ mM of the Q2 variant, however, the E2 layer outperforms the EEE2 core in recruiting the Q2 VLPs, and Q2 layers start enveloping the E2 layers formed around the EEE2 cores. The Q2-Q2 self PCF as well as the EEE2-Q2 and E2-Q2 cross PCFs indicate that the multilayered core-shell structures are ordered.

A layer comprising the P22-K2 VLPs starts forming around the multilayered EEE2-E2-Q2 aggregates upon further reduction in $I$ to 125 mM, and gets completed as $I$ is dialyzed down to the K2 variant threshold $I_t^{K2} = 75$ mM. The self and cross PCFs at 75 mM reflect a high degree of order characterizing each layer of the multilayered VLP aggregates, as well as across different layers.

The simulation findings are consistent with the experimental results obtained using fluorescence microscopy (right column)[56]. The image for $I$ just below $I_t^{EEE2}$ shows only a cluster of EEE2 VLPs. As $I$ is dialyzed down to a value near and below the respective threshold of the smaller-charged variants, only the VLPs associated with that variant type form a layer enveloping the core. For $I \lesssim I_t^{K2}$, a three-layer structure enveloping the EEE2 core is observed with the layers arranged outwards from the core in the order of decreasing variant charge.

Figure S14 in the SI illustrates the assembly products obtained using rapid dilution, starting from the same fluid-like state at 600 mM. The SI also provides the associated PCFs (Figs. S15 and S16). An exclusive assembly of EEE2 VLPs into ordered aggregates occurs as $I$ is decreased rapidly to 500 mM, which is identical to the first step via dialysis. Exclusive aggregation of EEE2 VLPs continues to occur until $\approx 350$ mM, however, the order decreases with decreasing $I$. In stark contrast to the emergence of core-shell structures produced via dialysis, rapid dilution to $I = 300$ mM leads to EEE2 and E2 VLPs mixing together into weakly-ordered amorphous aggregates. At $I = 245$ mM, the correlation between EEE2 & Q2 VLPs and between E2 & Q2 VLPs begins to emerge, and grows stronger with decreasing $I$, leading to kinetically-trapped aggregates with a mixed composition of EEE2, E2, and Q2 VLPs at $I = 200$ and 150 mM. Finally, for $I = 125$ and 75 mM, VLPs belonging to all four P22 variants are observed to mix together into amorphous aggregates characterized with weak long-range order.

Overall, these findings are consistent with the results obtained for two- and three-component mixtures. Decreasing the ionic strength via dialysis establishes an electrostatic drive to selectively assemble VLPs of only a single variant type into a core or a shell, leading to the hierarchical assembly of multilayered core-shell structures. However, if the ionic strength is decreased via rapid dilution, kinetically-trapped clusters with a mixed composition of VLPs of different types are formed. The presence of a higher-charged VLP variant continues to influence the assembly behavior of the VLPs associated with the lower-charge variants above their respective ionic strength thresholds.

### 3.5 Assembly mechanisms: Bound and Bridging Linkers

To explore the mechanisms driving the macroassembly of VLPs, the number of bound (condensed) and bridging dendrimers associated with different variants were extracted. A condensed dendrimer is defined as a dendrimer within 1.05 times the touch distance $r_T$ between a VLP and a dendrimer. A bridging dendrimer is defined as a condensed dendrimer shared between multiple VLPs[29] of either the same or different variant types.

Figure 11(a) shows the average number of condensed dendrimers $N_c$ per VLP vs the ionic strength $I$ for the steady-state assembly products produced via rapid dilution for the one-component systems. Overall, the results are consistent with our previous findings on E2, Q2, and K2 variants[29]. $N_c$ rises sharply for each variant as $I$ is decreased to the respective ionic strength threshold $I_t$, which is associated with the formation of ordered VLP arrays. $N_c$ is about the same for all variants at their respective $I_t$, and continues to rise with decreasing $I < I_t$, indicating an enhancement in the dendrimer recruitment capacity of the VLPs. However, for $I \ll I_t$, a small drop in $N_c$ is observed attributable to the over-condensation of dendrimers on the VLP surface, as described in detail in our earlier work[29].

Figure 11(b) shows the average number of bridging dendrimers $N_b$ vs the scaled ionic strength $I/I_t$ for each P22 variant. For all variants, $N_b$ exhibits a sharp rise as $I$ is decreased to $I_t$. For $I/I_t < 1$, $N_b$ increases with decreasing $I$, before decreasing sharply for much smaller values of the ionic strength $I \ll I_t$, for which we observe the disappearance of large VLP aggregates (Figure 2).

These findings indicate that the macroassembly of VLPs is driven by a sufficiently strong electrostatic attraction between a VLP and a dendrimer that enables the recruitment of condensed dendrimers to act as bridges between the VLPs. On the other hand, at low $I \ll I_t$ values reached via rapid dilution, the strong VLP-dendrimer attraction causes rapid recruitment of dendrimers which drives non-optimal bridging of VLPs by dendrimers such that the VLPs get kinetically-trapped into small clusters and the timescale to rearrange to form ordered aggregates becomes pro-

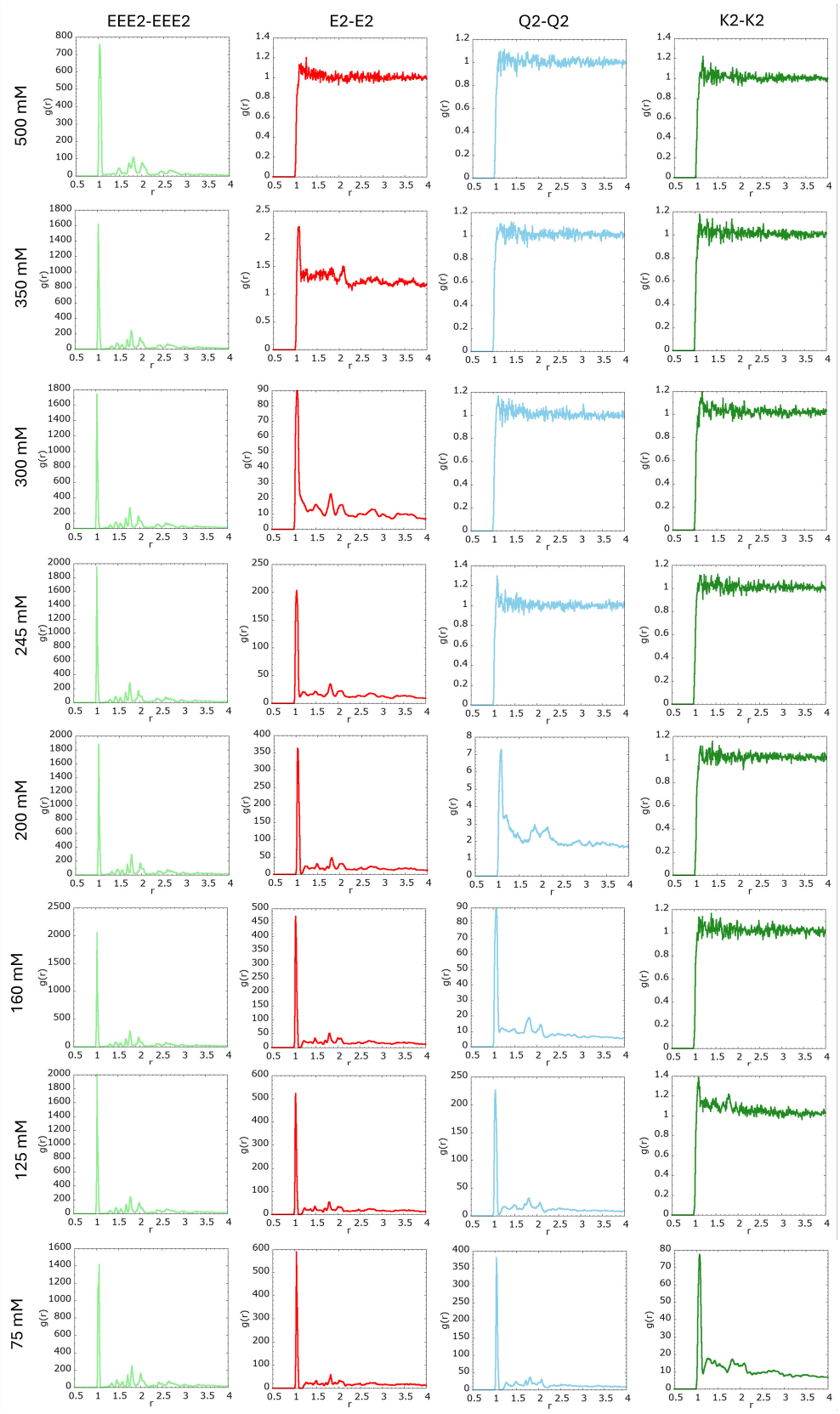


Fig. 9 Self pair correlation functions (PCFs) characterizing the assembly products generated via salt dialysis of a four-component mixture of P22-EEE2, P22-E2, P22-Q2 VLPs, and P22-K2 VLPs at the ionic strengths noted on the left. The first, second, third, and fourth columns show the EEE2-EEE2 (green), E2-E2 (red), Q2-Q2 (blue), and K2-K2 (dark green) PCFs respectively.

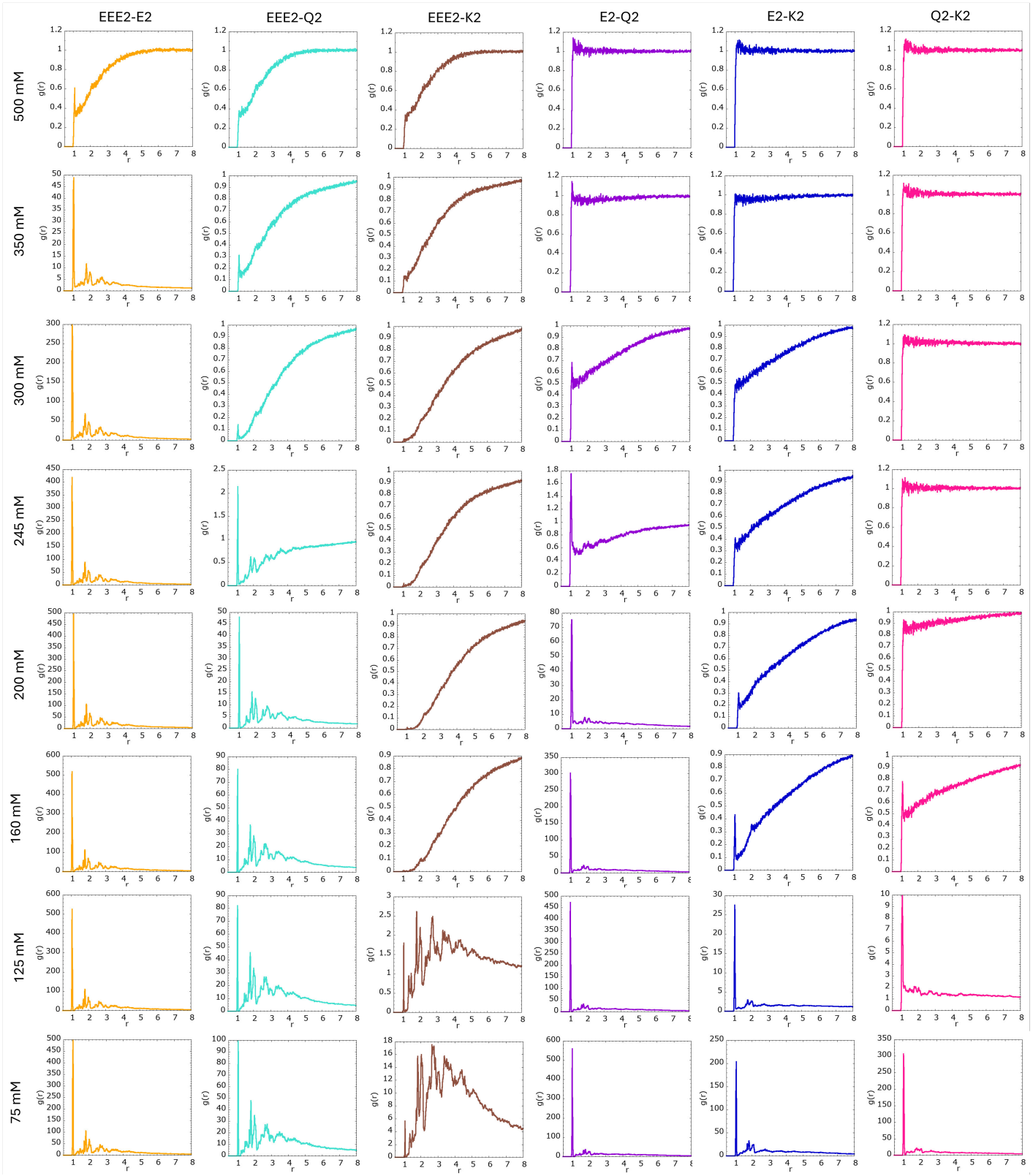


Fig. 10 Cross pair correlation functions for the variant-pair indicated at the top associated with the assembly products of the four-component mixture of P22-EEE2, P22-E2, P22-Q2, and P22-K2 VLPs generated via dialysis at the noted ionic strengths (left).

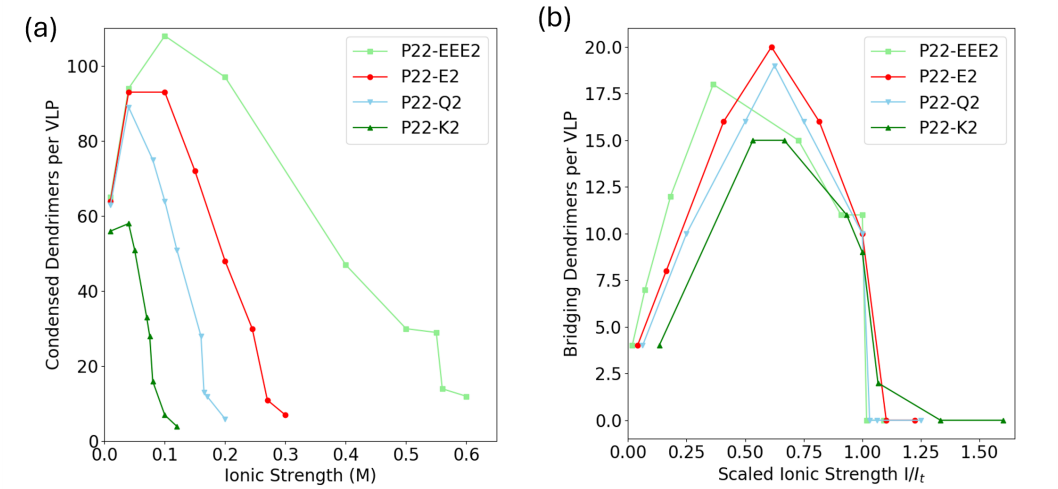


Fig. 11 Average number of condensed and bridging dendrimers per VLP for one-component systems. (a) Condensed dendrimers per VLP vs ionic strength $I$ for different P22 variants. (b) Bridging dendrimers per VLP vs scaled ionic strength $I/I_t$ where $I_t$ is the variant's ionic strength threshold.

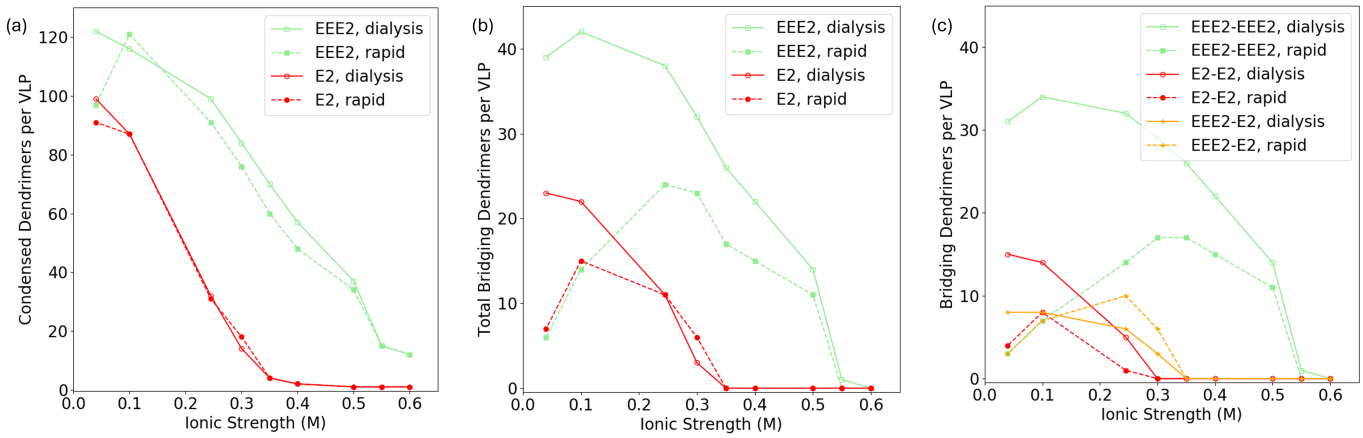


Fig. 12 Average number of condensed and bridging dendrimers per VLP vs ionic strength $I$ for the two-component EEE2-E2 mixture. Solid and dashed lines indicate dialysis and rapid dilution results respectively. (a) Condensed dendrimers associated with an EEE2 VLP (green) and an E2 VLP (red). (b) Total bridging dendrimers per EEE2 (green) and E2 (red) VLP. (c) Self-bridging dendrimers linking EEE2 VLPs (red) and E2 VLPs (green), and cross-bridging dendrimers crosslinking EEE2 and E2 VLPs (orange).

hibitively long. In our earlier work, we showed that ordered aggregates can persist at these lower ionic strengths if one starts with ordered arrays formed at $I \approx I_t$ and dialyzes out the salt[29]. Starting with an ordered array of VLPs and using a dialysis approach to lower the ionic strength is tantamount to reducing the timescale for VLP array formation to values comparable to the dendrimer recruitment timescale. We extend this analysis to mixtures of multiple P22 variants, and explore the implications of using different modes of modulating the solution's ionic strength on the linker distributions and associated macroassembly of VLPs.

We use the 2-component mixture of P22-EEE2 and P22-E2 discussed in section 3.2 to illustrate the general features of the linker distributions associated with the multicomponent systems. Figure 12(a) shows the average number of condensed dendrimers $N_c$ associated with the EEE2 (green) and E2 (red) VLPs as a function of $I$. Solid lines are dialysis results and dashed lines correspond to rapid dilution. The higher-charged EEE2 VLPs recruit more dendrimers compared to E2 VLPs at all $I$ values, regardless of whether $I$ was reached using dialysis or rapid dilution. This signals that the dendrimer recruitment potential increases with VLP charge, which is consistent with one-component systems. Interestingly, changing the mode of reducing the ionic strength produces minimal variation in $N_c$ for either variants. In other words, the ordered core-shell macrostructures and the amorphous aggregates with a mixed composition of VLPs are characterized with a similar average number of condensed dendrimers. These trends in $N_c$ vs $I$ are observed across all probed mixtures (Fig. S17).

The impact of using dialysis vs rapid dilution to change the ionic strength becomes apparent in Fig. 12 (b), which shows the average total number of bridging dendrimers $N_b$ vs $I$. For both EEE2 and E2 variants, rapid dilution and dialysis produce entirely different $N_b$ vs $I$ curves for $I$ less than their respective threshold $I_t$ (recall that $I_t^{\mathrm{EEE2}} = 550$ mM and $I_t^{\mathrm{E2}} = 245$ mM). In the case of rapid dilution, $N_b$ rises initially with decreasing $I$ before saturating and falling sharply as $I \ll I_t$, following a pattern similar to the one-component systems (Figure 11). In stark contrast, dialysis circumvents the early saturation as VLPs continue to recruit dendrimers to form bridging sites, causing $N_b$ to rise with decreasing $I$ over a wide range before saturating at very low $I$.

Differences in $N_b$ vs $I$ are also observed for $I > I_t$, depending on the variant's position in the charge hierarchy within the mixture. For the highest-charged variant (in this instance, EEE2), the $N_b$ vs $I$ curves from dialysis and rapid dilution approaches coincide. However, for the P22-E2 variant, $N_b$ is higher for rapid dilution compared to dialysis, indicating that E2 VLPs recruit more dendrimers to bridge with other VLPs (of either variants) when the ionic strength is reduced abruptly. Indeed, comparing the simulation snapshots in Figures 3 and 4 at 300 mM, there are more P22-E2 VLPs still in solution in the dialysis case when compared to the rapid dilution case. This effect, present for all lower-charged variants in a mixture, becomes more pronounced the lower the variant is in the charge hierarchy of the mixture (Fig. S18).

In analyzing the role of bridging linkers in mixtures of multiple types of NPs, it is useful to distinguish between bridging linkers that link NPs of the same type vs those that "cross-link" NPs of different types. Figure 12c shows these self and cross bridging linkers for the two-component EEE2-E2 system. We can now attribute the higher $N_b$ in Figure 12 (b) associated with the E2 variant in the case of rapid dilution compared to dialysis for $I = 300$ mm $> I_t^{E2}$ to the large number of cross bridging dendrimers between E2 and EEE2 VLPs. Under these solution conditions, VLPs co-assemble into mixed-composition aggregates via rapid dilution, leading to more contact sites between EEE2 and E2 VLPs, as evident in Figure 4, compared to dialysis, where only the EEE2 VLPs at the edge of the core can share the cross-bridging dendrimers with E2 VLPs. Moreover, we also observe that while the total number of bridging dendrimers are similar for the case of rapid dilution and dialysis at $I \sim I_t^{E2}$, dialysis produces higher self bridging dendrimers than rapid dilution while rapid dilution leads to higher cross bridging dendrimers. More importantly, the number of self bridging dendrimers exceed significantly compared to cross bridging dendrimers as $I$ is reduced using dialysis, compared to rapid dilution where they are similar. We link this excess of self bridging compared to cross linking as critical to the formation of core-shell structures. Other mixtures also yielded comparable results for these self and cross bridging dendrimers (Fig. S19).

The bound and bridging dendrimer data associated with different mixtures acquired from simulations can be used to assess the effect of the presence of higher-charged VLPs on the assembly behavior of the lower-charged VLPs in a mixture. Figure 13 illustrates this, by showing the results of condensed $N_c$ and total bridging $N_b$ dendrimers associated with the P22-E2 variant, which is present in all the mixtures studied. Figure 13a shows $N_c$ vs $I$ for both dialysis (solid lines) and rapid dilution (dashed lines) cases. No significant difference is observed between the two different methods of ionic strength reduction, in agreement with the results from Figure 12. Further, for $I < I_t^{\mathrm{E2}} = 245$ mM, no clear separation between the different trendlines is present. However, for $I > I_t^{E2}$, the $N_c$ vs $I$ curves separate into two branches. In mixtures with E2 as the highest charge variant, $N_c$ decreases sharply with increasing $I$ above $I_t^{E2}$ similar to the case of the one-component E2 system (black dashed line) indicating that the lower-charged VLPs do not have considerable effect on the dendrimer recruitment potential of the highest-charged variant. Note that in these cases, simulations were only performed until 300 mM, as above this concentration all VLPs remain dispersed in the solution and are associated with a negligible amount of condensed dendrimers. On the other hand, in mixtures containing P22-EEE2 VLPs, which have a higher charge than P22-E2 VLPs, $N_c$ exhibits a gradual decline with increasing $I$ and we observe a significant number of condensed dendrimers on the surface of the E2 VLPs at 300 mM.

A similar grouping of mixtures into two separate branches is observed for $I > I_t^{E2}$ for the bridging dendrimers in both dialysis (Fig. 13b) and rapid dilution cases (Fig. 13c). In mixtures where E2 is the highest-charged variant, $N_b$ decreases sharply to 0 as $I$ is increased beyond $I_t^{E2}$. However, in mixtures where EEE2 VLPs are present, $N_b$ exhibits a gradual decrease with increasing $I$. We attribute the enhancement in the dendrimer recruitment potential of the lower-charged VLPs at $I > I_t$ to the presence of the dendrimers bound to the higher-charged VLPs. The strong electrostatic attraction between these dendrimers and the lower-charged VLPs results in the changes in their assembly behavior.

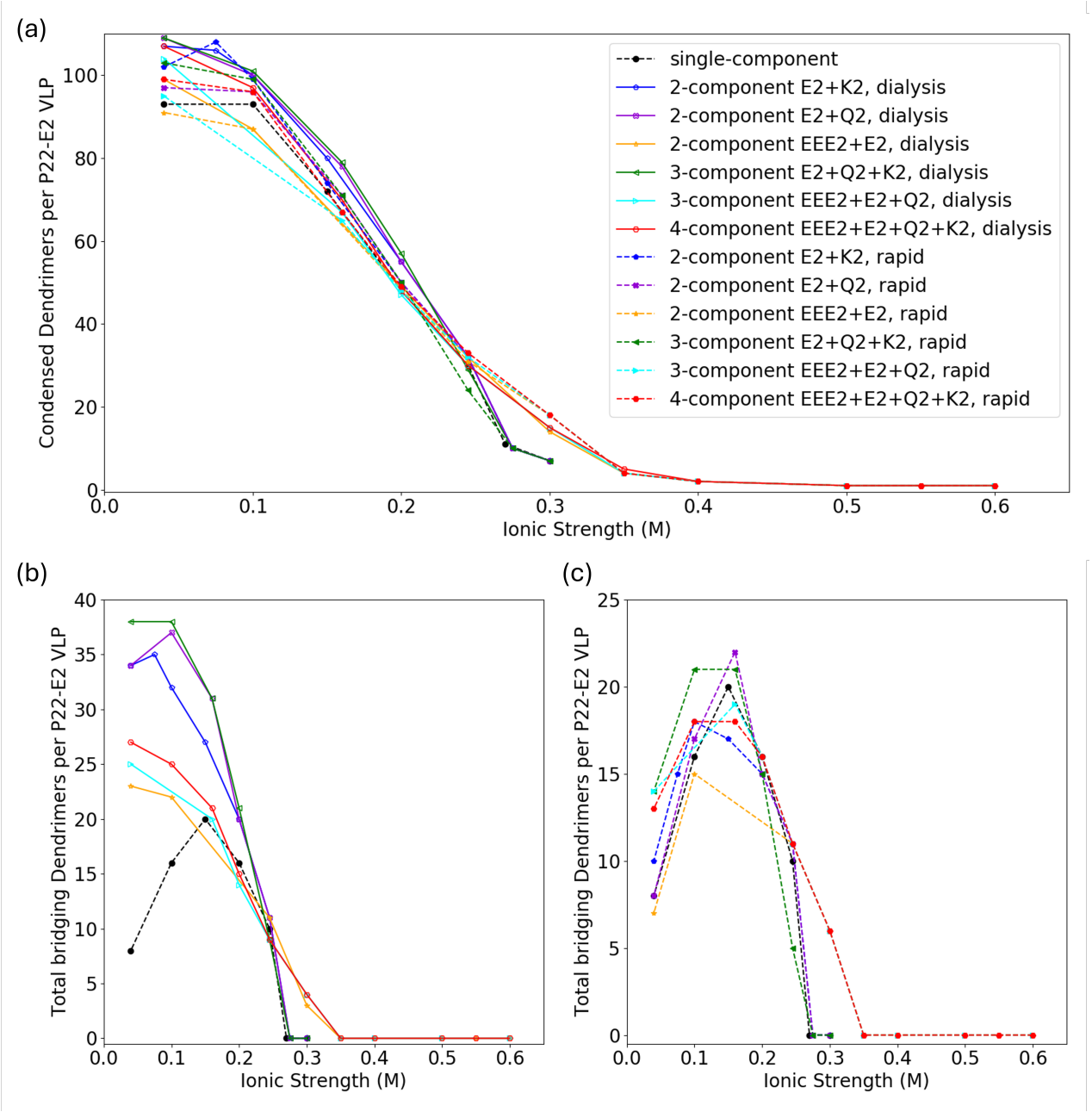


Fig. 13 Average number of condensed and total bridging dendrimers per E2 VLP vs ionic strength $I$ for the mixtures noted in the legend in (a) involving the P22-E2 variant. Solid and dashed lines indicate dialysis and rapid dilution results respectively. (a) Condensed dendrimers per E2 VLP. (b) Total bridging dendrimers per E2 VLP for the dialysis cases. Black dashed line represents the rapid dilution result for the one-component E2 system, and is shown for reference. (c) Total bridging dendrimers per E2 VLP for the rapid dilution cases.

In the absence of the higher-charged VLPs, entropic forces drive these dendrimers to remain dispersed in the solution.

## Conclusions

Protein cages such as VLPs have emerged as attractive building blocks for engineering synthetic self-assembled systems. VLPs derived from P22 bacteriophage can be genetically engineered to create variants of different surface charges. We investigated the self-assembly of single and multiple types of P22 VLPs mixed with oppositely-charged linkers (dendrimers) in aqueous electrolyte solutions using an experimentally-informed coarse-grained model validated across a broad range of NP charge and ionic strength.

The model accurately captured the self-assembly behavior of single-component systems, in particular the assembly states of higher-charged P22-EEE2 VLPs that were inaccessible with earlier models[29,56], over a broad range of ionic strength. All four P22 variants assembled into ordered arrays when $I$ was lowered below an ionic strength threshold $I_t$ that increased with increasing variant charge, consistent with experiments. The well separated threshold ionic strengths for different variants enabled a dialysis approach where decreasing ionic strength initiates assembly of only one specific type of VLPs. MD simulations of VLP mixtures containing two, three, and four types of VLPs revealed that this dialysis approach can lead to the self-assembly of VLPs into ordered multilayered core-shell arrays with each layer comprising VLPs of a single variant type. Simulation results were validated by fluorescence microscopy and SAXS experiments.

The method of ionic strength adjustment—either through rapid dilution or salt dialysis—profoundly influenced the recruitment of dendrimers and the resulting self-assembled structure. A gradual reduction in the salt concentration of the solution via dialysis facilitated the formation of core-shell structures with the highest-charged VLPs forming the core and other VLPs self-assembling into layers around this core in order of decreasing VLP surface charge outward from the core. The sequential aggregation of different P22 variants into layered structures with decreasing ionic strength was associated with the rise in the number of bridging dendrimers. Furthermore, the self and cross VLP-VLP pair correlation functions showed that dialysis promoted the creation of ordered aggregates with FCC/HCP lattice structure. Conversely, rapid dilution produced amorphous aggregates of mixed composition characterized with lower degrees of order, which was linked to the saturation and decline of bridging dendrimers due to the abrupt reduction of the solution's ionic strength. The multilayered core-shell structures assembled via dialysis and the mixed aggregates formed via rapid dilution can inform the design of complex VLP-based materials with tailored functionalities for use in biomedical and catalysis applications.

Simulations showed that, regardless of dialysis or rapid dilution, higher-charged VLPs in a mixture can alter the assembly behavior of lower-charged VLPs above their ionic strength threshold $I_t$, where as part of a single-component system they exhibit no aggregation. Strong correlations between lower-charged VLPs and higher-charged VLPs at ionic strengths up to a 100 mM higher than $I_t$ were observed, which were a precursor to the assembly of lower-charged VLPs at $I > I_t$ into ordered layers around the preformed cores in the case of dialysis or into mixed co-aggregates in the case of rapid dilution. This aggregation of lower-charged VLPs is accompanied by a rise in the condensed and bridging dendrimers associated with these VLPs, and can be attributed to the stronger localization of dendrimers by the higher-charge VLPs. This behavior underlines the importance of the oppositely-charged linkers in the self-assembly process, providing further insight into the design of sophisticated VLP constructs.

We have demonstrated an approach based on salt dialysis to generate and control the hierarchical assembly of charged NPs into layered materials from a one-pot synthesis of multiple types of NPs. The principles and mechanisms elucidated here are broadly applicable to the self-assembly of diverse NPs mediated by electrostatic interactions, offering a framework for creating complex structures from nanoscale building blocks that respond to changes in ionic strength. Overall, these findings contribute significantly to the understanding and development of self-assembled materials, paving the way for future advancements in the broader field of soft-matter-based nanotechnology.

## Author contributions

C.F.d.L. and V.J. developed the model and analyzed the simulation data. C.F.d.L performed simulations and prepared visualizations. N. H. and M. U performed experiments. M. U., T. D. and V. J. conceptualized the ideas. T.D. and V. J. supervised the project. C.F.d.L. and V.J. wrote the original draft. C.F.d.L., M.U., T.D., and V.J. reviewed and edited the manuscript.

## Conflicts of interest

There are no conflicts to declare

## Data availability

The data supporting this article have been included as part of the Supplementary Information.

## Acknowledgements

This work was supported by National Science Foundation through Grant DMR Nos. DMR-1753182 and CMMI-1922883.

## Notes and references

1 G. M. Whitesides and B. Grzybowski, *Science*, 2002, **295**, 2418–2421.
2 M. Uchida, M. T. Klem, M. Allen, P. Suci, M. Flenniken, E. Gillitzer, Z. Varpness, L. O. Liepold, M. Young and T. Douglas, *Advanced Materials*, 2007, **19**, 1025–1042.
3 D. Hayakawa, T. E. Videbaek, D. M. Hall, H. Fang, C. Sigl, E. Feigl, H. Dietz, S. Fraden, M. F. Hagan, G. M. Grason *et al.*, *Proceedings of the National Academy of Sciences*, 2022, **119**, e2207902119.
4 A. C. Mendes, E. T. Baran, R. L. Reis and H. S. Azevedo, *WIREs Nanomedicine and Nanobiotechnology*, 2013, **5**, 582–612.
5 D. Philp and J. F. Stoddart, *Angewandte Chemie International Edition in English*, 1996, **35**, 1154–1196.
6 R. Klajn, J. F. Stoddart and B. A. Grzybowski, *Chem. Soc. Rev.*, 2010, **39**, 2203–2237.

7 S. Mann, *Nature materials*, 2009, **8**, 781–792.

8 M. A. Kostiainen, P. Hiekkataipale, J. A. de la Torre, R. J. Nolte and J. J. Cornelissen, *Journal of Materials Chemistry*, 2011, **21**, 2112–2117.

9 D. H. Gracias, J. Tien, T. L. Breen, C. Hsu and G. M. Whitesides, *Science*, 2000, **289**, 1170–1172.

10 Z. Cai, Z. Li, S. Ravaine, M. He, Y. Song, Y. Yin, H. Zheng, J. Teng and A. Zhang, *Chem. Soc. Rev.*, 2021, **50**, 5898–5951.

11 C. T. Black, *Applied Physics Letters*, 2005, **87**, 163116.

12 B. A. Grzybowski, C. E. Wilmer, J. Kim, K. P. Browne and K. J. Bishop, *Soft Matter*, 2009, **5**, 1110–1128.

13 H. Hu, M. Gopinadhan and C. O. Osuji, *Soft matter*, 2014, **10**, 3867–3889.

14 A. Rao, S. Roy, V. Jain and P. P. Pillai, *ACS Applied Materials & Interfaces*, 2022, **15**, 25248–25274.

15 S. C. Glotzer, M. J. Solomon and N. A. Kotov, *AIChE Journal*, 2004, **50**, 2978–2985.

16 D. Nykypanchuk, M. M. Maye, D. Van Der Lelie and O. Gang, *Nature*, 2008, **451**, 549–552.

17 R. J. Macfarlane, B. Lee, M. R. Jones, N. Harris, G. C. Schatz and C. A. Mirkin, *Science*, 2011, **334**, 204–208.

18 K. Tao, P. Makam, R. Aizen and E. Gazit, *Science*, 2017, **358**, eaam9756.

19 A. Kuzyk, R. Schreiber, Z. Fan, G. Pardatscher, E.-M. Roller, A. Högele, F. C. Simmel, A. O. Govorov and T. Liedl, *Nature*, 2012, **483**, 311–314.

20 H. Xiong, M. Y. Sfeir and O. Gang, *Nano letters*, 2010, **10**, 4456–4462.

21 Y. Zhang, F. Lu, K. G. Yager, D. Van Der Lelie and O. Gang, *Nature nanotechnology*, 2013, **8**, 865–872.

22 J. A. Fan, Y. He, K. Bao, C. Wu, J. Bao, N. B. Schade, V. N. Manoharan, G. Shvets, P. Nordlander, D. R. Liu and F. Capasso, *Nano Letters*, 2011, **11**, 4859–4864.

23 M. R. Jones, N. C. Seeman and C. A. Mirkin, *Science*, 2015, **347**, 1260901.

24 T. D. Nguyen, E. Jankowski and S. C. Glotzer, *ACS nano*, 2011, **5**, 8892–8903.

25 S. C. Glotzer, *Chemical Engineering Science*, 2015, **121**, 3 – 9.

26 P. Akcora, H. Liu, S. K. Kumar, J. Moll, Y. Li, B. C. Benicewicz, L. S. Schadler, D. Acehan, A. Z. Panagiotopoulos, V. Pryamitsyn *et al.*, *Nature materials*, 2009, **8**, 354–359.

27 C. Chen, R. A. Wylie, D. Klinger and L. A. Connal, *Chemistry of Materials*, 2017, **29**, 1918–1945.

28 M. Uchida, K. McCoy, M. Fukuto, L. Yang, H. Yoshimura, H. M. Miettinen, B. LaFrance, D. P. Patterson, B. Schwarz, J. A. Karty *et al.*, *ACS nano*, 2018, **12**, 942–953.

29 N. E. Brunk, M. Uchida, B. Lee, M. Fukuto, L. Yang, T. Douglas and V. Jadhao, *ACS Applied Bio Mat.*, 2019, **2**, 2192–2201.

30 J. D. Hartgerink, E. Beniash and S. I. Stupp, *Science*, 2001, **294**, 1684–1688.

31 C. Gao, S. Kewalramani, D. M. Valencia, H. Li, J. M. McCourt, M. O. De La Cruz and M. J. Bedzyk, *Proceedings of the National Academy of Sciences*, 2019, **116**, 22030–22036.

32 M. A. Kostiainen, O. Kasyutich, J. J. Cornelissen and R. J. Nolte, *Nature Chemistry*, 2010, **2**, 394–399.

33 S. Palchoudhury, Z. Zhou, K. Ramasamy, F. Okirie, P. E. Prevelige and A. Gupta, *Journal of Materials Research*, 2016, **32**, 465–472.

34 M. Künzle, T. Eckert and T. Beck, *Journal of the American Chemical Society*, 2016, **138**, 12731–12734.

35 A. Korpi, E. Anaya-Plaza, S. Välimäki and M. Kostiainen, *Wiley Interdisciplinary Reviews: Nanomedicine and Nanobiotechnology*, 2020, **12**, e1578.

36 J. R. McMillan, O. G. Hayes, P. H. Winegar and C. A. Mirkin, *Accounts of chemical research*, 2019, **52**, 1939–1948.

37 K. Matsuurua, *RSC Advances*, 2014, **4**, 2942–2953.

38 T. Douglas and M. Young, *Science*, 2006, **312**, 873–875.

39 B. Schwarz, M. Uchida and T. Douglas, *Advances in virus research*, 2017, **97**, 1–60.

40 W. M. Aumiller, M. Uchida and T. Douglas, *Chemical Society Reviews*, 2018, **47**, 3433–3469.

41 T. G. Edwardson and D. Hilvert, *Journal of the American Chemical Society*, 2019, **141**, 9432–9443.

42 Z. Chen, N. Li, L. Chen, J. Lee and J. J. Gassensmith, *Small*, 2016, **12**, 4563–4571.

43 A. J. Vaidya and K. V. Solomon, *ACS Applied Bio Materials*, 2022, **5**, 1980–1989.

44 J. He, L. Yu, X. Lin, X. Liu, Y. Zhang, F. Yang and W. Deng, *Viruses*, 2022, **14**, 1905.

45 J. Sun, C. DuFort, M.-C. Daniel, A. Murali, C. Chen, K. Gopinath, B. Stein, M. De, V. M. Rotello, A. Holzenburg *et al.*, *Proceedings of the National Academy of Sciences*, 2007, **104**, 1354–1359.

46 M. Uchida, B. LaFrance, C. C. Broomell, P. E. Prevelige Jr and T. Douglas, *Small*, 2015, **11**, 1562–1570.

47 M. A. Kostiainen, P. Hiekkataipale, A. Laiho, V. Lemieux, J. Seitsonen, J. Ruokolainen and P. Ceci, *Nature nanotechnology*, 2013, **8**, 52–56.

48 B. Zheng, K. Zhou, T. Zhang, C. Lv and G. Zhao, *Nano Letters*, 2019, **19**, 4023–4028.

49 E. Strable, J. E. Johnson and M. Finn, *Nano letters*, 2004, **4**, 1385–1389.

50 Y. Tian, J. R. Lhermitte, L. Bai, T. Vo, H. L. Xin, H. Li, R. Li, M. Fukuto, K. G. Yager, J. S. Kahn *et al.*, *Nature materials*, 2020, **19**, 789–796.

51 K. McCoy, M. Uchida, B. Lee and T. Douglas, *ACS nano*, 2018, **12**, 3541–3550.

52 R. Asor, O. Ben-nun Shaul, A. Oppenheim and U. Raviv, *ACS nano*, 2017, **11**, 9814–9824.

53 G. J. Bedwell, Z. Zhou, M. Uchida, T. Douglas, A. Gupta and P. E. Prevelige, *Biomacromolecules*, 2015, **16**, 214–218.

54 D. P. Patterson, P. E. Prevelige and T. Douglas, *ACS nano*, 2012, **6**, 5000–5009.

55 P. C. Jordan, D. P. Patterson, K. N. Saboda, E. J. Edwards, H. M. Miettinen, G. Basu, M. C. Thielges and T. Douglas, *Nature chemistry*, 2016, **8**, 179–185.

56 M. Uchida, N. E. Brunk, N. D. Hewagama, B. Lee, P. E. Prevelige Jr, V. Jadhao and T. Douglas, *ACS nano*, 2022, **16**, 7662–

7673.
57 R. Esfand and D. A. Tomalia, *Drug discovery today*, 2001, **6**, 427–436.
58 S. Alexander, P. Chaikin, P. Grant, G. Morales, P. Pincus and D. Hone, *The Journal of chemical physics*, 1984, **80**, 5776–5781.
59 J. C. Crocker and D. G. Grier, *Physical review letters*, 1996, **77**, 1897.
60 M. Aubouy, E. Trizac and L. Bocquet, *Journal of Physics A: Mathematical and General*, 2003, **36**, 5835.
61 S. Brittman, N. A. Mahadik, S. B. Qadri, P. Y. Yee, J. G. Tischler and J. E. Boercker, *ACS Applied Materials & Interfaces*, 2020, **12**, 24271.
62 G. Lin, S. W. Chee, S. Raj, P. Král and U. Mirsaidov, *ACS Nano*, 2017, **10**, 7443–7450.
63 G. I. Guerrero-García, P. González-Mozuelos and M. Olvera de la Cruz, *ACS Nano*, 2013, **7**, 9714–9723.
64 N. Boon, G. I. Guerrero-García, R. van Roij and M. Olvera de la Cruz, *Proceedings of the National Academy of Sciences*, 2015, **112**, 9242–9246.
65 R. Zandi, B. Dragnea, A. Travesset and R. Podgornik, *Physics Reports*, 2020, **847**, 1–102.
66 S. Li, G. Erdemci-Tandogan, J. Wagner, P. Van Der Schoot and R. Zandi, *Physical Review E*, 2017, **96**, 022401.
67 S. Plimpton, *Journal of Computational Physics*, 1995, **117**, 1–19.
68 J. A. van Meel, L. Filion, C. Valeriani and D. Frenkel, *The Journal of chemical physics*, 2012, **136**, 234107.

## Data Availability Statement

The data supporting this article have been included as part of the Supplementary Information.